A New Bulk Microphysical Scheme That Includes Riming Intensity and Temperature-Dependent Ice Characteristics

YANLUAN LIN* AND BRIAN A. COLLE

School of Marine and Atmospheric Sciences, Stony Brook University, Stony Brook, New York

(Manuscript received 25 November 2009, in final form 13 August 2010)

ABSTRACT

A new bulk microphysical parameterization (BMP) scheme is presented that includes a diagnosed riming intensity and its impact on ice characteristics. As a result, the new scheme represents a continuous spectrum from pristine ice particles to heavily rimed particles and graupel using one prognostic variable [precipitating ice (PI)] rather than two separate variables (snow and graupel). In contrast to most existing parameterization schemes that use fixed empirical relationships to describe ice particles, general formulations are proposed to consider the influences of riming intensity and temperature on the projected area, mass, and fall velocity of PI particles. The proposed formulations are able to cover the variations of empirical coefficients found in previous observational studies. The new scheme also reduces the number of parameterized microphysical processes by ~50% as compared to conventional six-category BMPs and thus it is more computationally efficient.

The new scheme (called SBU-YLIN) has been implemented in the Weather Research and Forecasting (WRF) model and compared with three other schemes for two events during the Improvement of Microphysical Parameterization through Observational Verification Experiment (IMPROVE-2) over the central Oregon Cascades. The new scheme produces surface precipitation forecasts comparable to more complicated BMPs. The new scheme reduces the snow amounts aloft as compared to other WRF schemes and compares better with observations, especially for an event with moderate riming aloft. Sensitivity tests suggest both reduced snow depositional growth rate and more efficient fallout due to the contribution of riming to the reduction of ice water content aloft in the new scheme, with a larger impact from the partially rimed snow and fallout.

1. Introduction

Ice particles have different properties and growth characteristics based on the ambient conditions (Korolev et al. 2000). Under different temperature and supersaturation conditions, ice particles grow into different habits and complex structures as summarized in Pruppacher and Klett (1997). These habits impact the ice particle's cross-sectional area, mass, and fall speed. In addition, because of the relatively small number of ice nuclei available and slow ice growth compared to the condensational growth (Pruppacher and Klett 1997), supercooled water exists at heights above the freezing level. In mixed phase clouds, riming also changes and modifies the ice particle properties.

The representation of ice particle properties is important, since it has wide applications ranging from the retrieval of ice water content using remote sensing (Mace et al. 2006; Heymsfield et al. 2008a) and in situ measurements (Heymsfield et al. 2002) to its parameterization in numerical models (Lin et al. 1983; Rutledge and Hobbs 1983; Thompson et al. 2004, 2008; among others). Many empirical formulas, such as power laws, have been derived to describe irregular shape ice particle properties, such as relating the projected area, mass, and fall velocity to the maximum dimension (e.g., Locatelli and Hobbs 1974; Mitchell et al. 1990; Heymsfield 2003; among others). However, the change in coefficients for the power laws with different environmental conditions has not been noted until recently (Barthazy and Schefold 2006; Baker and Lawson 2006; Heymsfield et al. 2007). A generalized description of

* Current affiliation: University Corporation for Atmospheric Research, Boulder, Colorado, and NOAA/Geophysical Fluid Dynamics Laboratory, Princeton, New Jersey.

Corresponding author address: Dr. Yanluan Lin, NOAA/Geophysical Fluid Dynamics Laboratory, Princeton University, Forrestal Campus, P.O. Box 308, Princeton, NJ 08540.
E-mail: yanluan.lin@noaa.gov

DOI: 10.1175/2010MWR3293.1

ice particle properties is needed in numerical models to represent more of the conditions associated with ice clouds.

There are a wide variety of bulk microphysical parameterizations (BMPs) available in version 3.1 of the Weather Research and Forecasting (WRF) model (Skamarock et al. 2005), ranging from the simple Kessler BMP to the newer Thompson (Thompson et al. 2008) and double-moment (Morrison et al. 2009) schemes. One key property in a BMP is the treatment of snow and graupel. Because of the large difference in fall velocity between snow and graupel (or hail), the residence time and fallout of precipitation depends highly on the partitioning of mass between snow and graupel (Colle et al. 2005; Lin and Colle 2009). Snow and graupel (and hail) are often treated as separate categories in traditional BMPs (Rutledge and Hobbs 1983; Lin et al. 1983). Most BMPs treat snow and graupel by assuming spherical particles with constant density and use an abrupt transition from snow to graupel, thus neglecting partially rimed particles (Lin et al. 1983; Rutledge and Hobbs 1983; Reisner et al. 1998; Hong et al. 2004; among others). However, in reality, ice particles have different habits, while riming modifies these characteristics.

Both ice habit and riming should be considered in BMPs in order to better represent ice-related processes. In general, there have been two approaches to include habits in BMPs. One is to increase the numbers of prognosed variables to simulate the different habits explicitly (Meyers et al. 1997; Kong and Yau 1997; Straka and Mansell 2005), while another approach is to estimate the preferred habit at each grid point based on the local conditions in the cloud (Meyers et al. 1997), which can be tracked by partitioning the snow category into different habit types (Woods et al. 2007). To consider partially rimed particles, Dudhia et al. (2008) proposed using the snow and graupel mass-weighted fall velocity for the sedimentation of snow and graupel in a six-category BMP in WRF (Hong and Lim 2006).

By separately predicting the ice mixing ratios acquired from ice deposition versus riming, the riming contribution to the mass and fall speed of snow can be calculated (Stoelinga et al. 2007). Using a similar approach, Morrison and Grabowski (2008) considered the variation of particle properties with particle size and rimed mass fraction. The approach is novel and has some advantages over conventional BMPs; however, it is limited to use a fixed mass–diameter relation for nonspherical particles. Particle size–dependent mass–dimension and projected area–dimension relationships also make the integration over the whole size spectrum complicated and the transition between different sizes unsmooth.

Snow overprediction aloft has been noted in several studies from the Improvement of Microphysical Parameterization through Observational Verification Experiment (IMPROVE-2) over the central Oregon Cascades (Garvert et al. 2005b; Colle et al. 2005; Milbrandt et al. 2008; Lin and Colle 2009; Milbrandt et al. 2010). Sensitivity tests from some of these studies have suggested that small changes to existing BMPs may not help snow overprediction because of the inherent limitations of some BMPs, such as fixed snow characteristics (mass and fall speed relationships) and an abrupt transition from snow to graupel. Recent work by Milbrandt et al. (2010) showed that a single-moment version of the multimoment scheme of Milbrandt and Yau (2005) reduced the snow aloft compared with the two-moment version for the 13–14 December IMPROVE-2 event (Garvert et al. 2005a,b; Colle et al. 2005). They also emphasize the importance of snow depositional growth parameterization on the simulated snow aloft and surface precipitation. To overcome these limitations in many BMPs, the current paper proposes a more flexible and general approach that considers both the temperature and riming impact on ice particle properties. With the introduction of a diagnosed riming intensity parameter in the BMP, a continuous spectrum from pristine ice to heavily rimed snow and graupel can be represented.

The new BMP is described in detail in section 2 along with some observational and theoretical justifications. The new scheme is tested in WRF model for two IMPROVE-2 cases in section 3. Section 4 gives a summary and conclusions.

2. Description of the new microphysical parameterization

a. Prognostic variables

The new State University of New York at Stony Brook BMP scheme (hereafter referred to as SBU-YLIN, but labeled as SUNY in all the figures) was developed using the Purdue–Lin scheme (Lin et al. 1983; Chen and Sun 2002) as a starting point, which includes the supersaturation adjustment from Tao et al. (1989). The SBU-YLIN scheme includes five prognostic mixing ratios: water vapor, cloud ice, precipitating ice (PI), cloud liquid water, and rain. Dry snow, rimed snow, and graupel are included in the PI category through the introduction of a varying riming intensity parameter. Since snow and graupel share the same category in this new scheme, they also share the same processes (deposition/sublimation and collision with other hydrometeors). As compared with other six-category single-moment schemes (Fig. 1), such as the Purdue–Lin (Chen and Sun 2002) and WRF single-moment microphysics (WSM6; Hong and Lim 2006) schemes, the new scheme reduces the number of microphysical processes from ~40 to less than 20 and computational time

by ~5% and ~20%, respectively. The source, sink, and conversion terms that are different from conventional BMPs are described in the appendix.

b. Precipitating ice

The new approach in the SBU-YLIN scheme is mainly in the treatment of precipitating ice particles, which have a variety of riming intensities. Both shape and riming can change the particle properties. Because of the irregular shapes involved, the geometry of ice particles is often described by introducing a maximum diameter or dimension D. Power laws have been widely used to describe the mass–diameter (M-D), area–diameter (A-D), and fall velocity–diameter (V-D) relationships for ice particles:

$$M = a_m D^{b_m}, \tag{1}$$

$$A = a_a D^{b_a}, \tag{2}$$

$$V = a_v D^{b_v}, \tag{3}$$

where a and b are empirical coefficients, which are constants in many BMPs (Lin et al. 1983; Rutledge and Hobbs 1983; Ferrier 1994; Tao and Simpson 1993; Schultz 1995; Reisner et al. 1998; Hong et al. 2004; Thompson et al. 2004, 2008; Morrison et al. 2005; among others). Heymsfield et al. (2007) collected aircraft observations from a wide range of temperatures (between −60° and 0°C) within ice clouds at middle and low latitudes and derived a linear dependence on temperature for the coefficients (a_m and b_m) in the M-D relationship in Eq. (1) [see Table 1 in Heymsfield et al. (2007)]. This linear dependence is an oversimplification of ice particle habit considering the complex dependence of habits on both temperature and supersaturation (Pruppacher and Klett 1997), but it does serve as a useful starting point to generalize temperature impacts on ice characteristics. Using data collected in wave clouds over the Colorado Front Range, Baker and Lawson (2006) reported the A-D relationships for three crystal types (rosette, irregular, and column; see their Table 4). These approaches were used in the SBU-YLIN scheme to help mimic some of the impacts of different snow characteristics in the M-D and A-D relationships without needing to partition the snow category in a BMP into different habits.

Riming depends on several factors, such as liquid water content (LWC), ice water content (IWC), ice habit, temperature, and vertical motion. Riming also depends on ice particle size and droplet size [e.g., riming efficiency is near zero for small (<30–100 microns) ice crystals]. Relatively few observations (Mosimann et al. 1994; Mosimann 1995) have been reported to describe the degree of riming. For modeling studies, rimed mass fraction has been used instead of the more subjective riming degree used in observational studies. Mosimann et al. (1994) proposed a relationship [their Eq. (16)] between the degree of riming and the rimed mass fraction for all crystal types, which shows a near-linear relation for the rimed mass fraction in the range of [0.2, 0.8]. We refer the rimed mass fraction as riming intensity (Ri) later in the paper. Although the dependence of cloud phase on temperature has been noted (Korolev et al. 2003), few studies have tried to parameterize Ri based on environmental conditions. Lin et al. (2011) proposed that Ri can be approximated by the ratio between riming growth rate and the sum of riming and ice depositional growth rate, assuming steady state and saturation with respect to water as riming occurs [their Eq. (4)]:

$$\mathrm{Ri} = \frac{P_{\mathrm{rim}}}{P_{\mathrm{rim}} + P_{\mathrm{dep}}} = \frac{1}{1 + \dfrac{F(T)}{\mathrm{LWC(IWC)}^{0.17}}} \approx \frac{1}{1 + \dfrac{6 \times 10^{-5}}{\mathrm{LWC(IWC)}^{0.17}}}. \tag{4}$$

Lin et al. (2011) showed that this parameterization provides a reasonable estimate of riming intensity when compared with independent estimates using Doppler velocities from a vertically pointing millimeter cloud radar (MMCR) over Oklahoma during the Department of Energy Atmospheric Radiation Measurement (ARM) program (Stokes and Schwartz 1994). This definition automatically bounds the Ri from 0 (pristine ice particles) to 1 (graupel). The value of Ri is only computed when both LWC and IWC are larger than a threshold of 0.01 g m^{-3}; otherwise, Ri is set to zero. More field observations will be utilized in the future to refine the Ri parameterization. Since rimed particles do not typically decrease their riming intensity as they fall through the cloud (i.e., riming is primarily a one-way process), Ri in each grid column in the model does not decrease downward from its maximum value in the column. This prevents the situation of Ri approaching zero as rimed particles fall out of the cloud. As a property of ice particles, riming intensity should follow the ice particle growth history and trajectory. Future work will compare Ri as in Morrison and Grabowski (2008) and Stoelinga et al. (2007), in which Ri is predicted at each point by separately predicting the ice mixing ratios acquired through water vapor deposition and through riming. Overall, a simple diagnosed Ri in this paper still provides a useful first step to explore its impacts.

Now we propose a general framework to represent the impact of riming and temperature on ice crystal properties (mass, projected area, and fall speed). In the M-D

relationship above [Eq. (1)], a_m can be considered as an effective density and b_m as a fractal dimension (Liu 1995). The roundness of particles generally increases with riming and b_m approaches 3 for a spherical particle. Mosimann et al. [1994, their Eq. (3)] found that the rimed mass is dependent on a fitted constant raised to a power determined by riming degree. Since the *M-D* in Eq. (1) also has mass raised to some power b_m, we assume Ri is linearly related with b_m in this new scheme (note the near-linear relation between riming degree and rimed mass fraction stated before). Ice particle fall velocity generally increases with degree of riming (e.g., Locatelli and Hobbs 1974; Barthazy and Schefold 2006). Equation (11) indicates a_m should be proportional to a higher order of Ri to ensure the dependence of a_v on Ri. We found that a_m proportional to Ri^2 gives a good match with the empirical *M-D* relations (e.g., Fig. 3a). In addition, a stronger dependence of a_m on Ri than b_m is also consistent with the strong dependence of ice particle density on riming in some observational studies (e.g., Mitchell et al. 1990). However, we acknowledge that this square dependence needs to be better quantified and refined in future work. More observations are needed to better quantify the proposed functional forms and coefficients in the future. More specifically, the first two terms in Eqs. (5) and (6) are from Heymsfield et al. (2007) and reflect the particle property changes as a function of ambient temperature in °C, while the last term reflects the riming effect:

$$a_m = c_0 + c_1 T + c_2 \mathrm{Ri}^2, \tag{5}$$

$$b_m = C_0 + C_1 T + C_2 \mathrm{Ri}. \tag{6}$$

We utilize the temperature-dependent *A-D* relationship derived by Baker and Lawson (2006) and include the effect of Ri to get

$$a_a = d_0 + d_1 T + d_2 \mathrm{Ri}, \tag{7}$$

$$b_a = D_0 + D_1 T + D_2 \mathrm{Ri}. \tag{8}$$

To our knowledge, there is no observational analysis of how riming impacts ice crystal projected area. For simplicity, we start with a simple linear dependence of a_a and b_a on riming intensity.

With the *M-D* and *A-D* relationships known, we follow the Best number X and Reynolds number Re approach to derive the *V-D* relationship (Mitchell 1996). This approach does not need an explicit drag coefficient and the fall speed is relatively independent of the particle habit after accounting for the dependence on the mass–projected area ratio (Mitchell 1996),

TABLE 1. Parameters (showing power-law coefficients in cgs units) used in the *A-D* and *M-D* relationships for the SBU-YLIN scheme.

Name	Value	Name	Value
c_0	0.004	C_0	1.85
c_1	6×10^{-5}	C_1	0.003
c_2	0.15	C_2	1.25
d_0	1.28	D_0	1.50
d_1	−0.012	D_1	0.0075
d_2	−0.6	D_2	0.50

$$\mathrm{Re} = aX^b = \frac{DV}{\nu}, \tag{9}$$

$$X = \frac{2gmD^2}{\rho_a \nu^2 A}, \tag{10}$$

where g is the gravitational acceleration constant, ρ_a is the air density, and ν is the kinematic viscosity of the air. Both $a = 1.08$ and $b = 0.499$ are from Mitchell (1996). Incorporating Eqs. (9) and (10) and using the *M-D* and *A-D* relationships defined in Eqs. (5)–(8), one obtains

$$a_v = a\nu\left(\frac{2ga_m}{\rho_a \nu^2 a_a}\right)^b, \tag{11}$$

$$b_v = b(b_m - b_a + 2) - 1. \tag{12}$$

We need to determine the parameters c_2, C_2, d_2, and D_2. First, C_2 and D_2 are determined to bound b_m and b_a by 3 and 2, respectively, by assuming $\mathrm{Ri} = 1$ for spherical particles. Second, previous studies (e.g., Hanesch 1999) suggest that the equivalent density of heavily rimed ice particles and graupel is around 200–300 kg m^{-3} and does not depend on particle size. From Eq. (1), equivalent density ρ_e is

$$\rho_e = \frac{6}{\pi} a_m D^{b_m - 3}. \tag{13}$$

If we apply an equivalent density of 300 kg m^{-3} and b_m of 3, we get $c_2 \sim 0.15$. Finally, we determine d_2 from Eq. (11) after applying the fall speed relationship for graupel ($V = 1.1D^{0.57}$, $M = 0.044D^{2.9}$) as in Locatelli and Hobbs (1974). Because of the relatively weak dependence of these coefficients on temperature (cf. Table 1), we use a representative temperature of −10°C and Ri of 0.85 [graupel in Locatelli and Hobbs (1974) is generally heavily rimed particles] in the derivation of d_2. Note that in the derivation of d_2 we have to ensure a_v, a_m, and b_m in a reasonable range simultaneously as compared to observations. These empirical constants in Eqs. (5)–(8) are shown in Table 1 to give the power-law coefficients in cgs units.

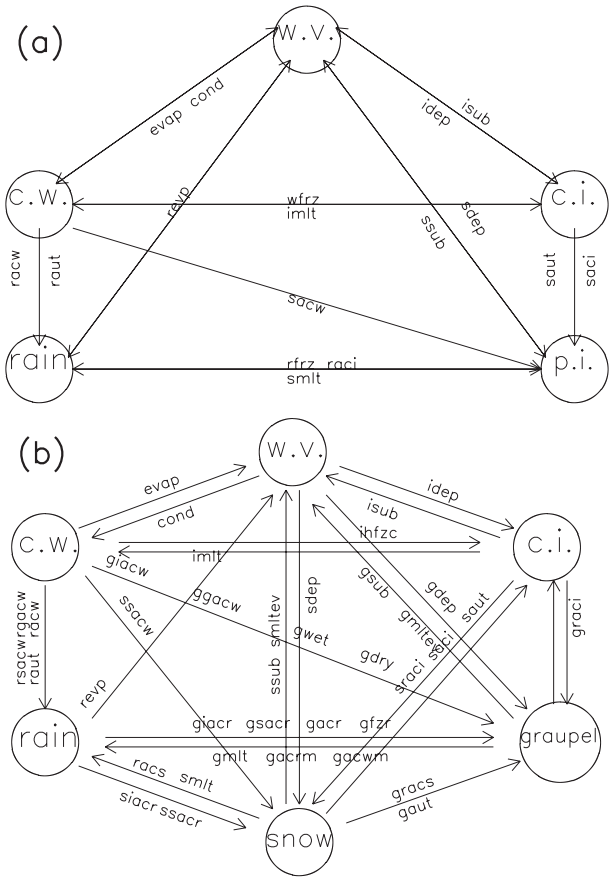

FIG. 1. (a) Microphysical flowchart showing the processes for the SBU-YLIN scheme. The circles represent the various water species (water vapor, cloud water, cloud ice, precipitating ice, and rain), and the arrows are the processes that link the various species (see the appendix for the description of some processes) and Colle and Zeng (2004) for the others. (b) As in (a), but for the Purdue–Lin scheme.

Figures 2a and 2b show the derived coefficients in the *A-D* and *M-D* relationships as Ri is varied from 0 to 1 and how they compare with those already in the literature (Locatelli and Hobbs 1974; Mitchell et al. 1990; Mitchell 1996; Barthazy and Schefold 2006). Note that Ri was not explicitly observed in these cited studies, so it was derived from the reported qualitative ''riming status'' according to Table 1 in Mosimann et al. (1994) and then converted to riming intensity using Eq. (16) in Mosimann et al. (1994). These formulations describe qualitatively well the observed increase of these coefficients with riming intensity. Spherical assumption (circle in Fig. 2a) is used widely in most BMPs to calculate the particle projected area. It gives larger a_a and b_a than those empirically derived (crosses in Fig. 2a), especially for lightly and moderately rimed particles. Since a_a and b_a are smaller than those for a spherical particle in other BMPs (circle in Fig. 2a), ice particles in the new scheme generally have smaller projected area than that of a spherical particle. For the ice mass (Fig. 2b), the spherical assumption with a density of 400 kg m^{-3} (upper circle in Fig. 2b), which is used widely for graupel in many BMPs (Reisner et al. 1998; Hong et al. 2004; Chen and Sun 2002; Thompson et al. 2004; among others), occurs within the upper bound of various densely rimed snow and graupel observations. Meanwhile, the spherical assumption with a density of 100 kg m^{-3} (lower circle in Fig. 2b), which is used widely for snow in BMPs (Lin et al. 1983; Reisner et al. 1998; Hong et al. 2004; Chen and Sun 2002; Thompson et al. 2004; among others), also overestimates the density of most ice particles, especially for lightly and moderately rimed particles. In addition, smaller empirical coefficients (double circle in Fig. 2b) from Brown and Francis (1995) also cannot represent the wide range of habits and riming intensity observed. With the temperature- and Ri-dependent coefficients, the scheme covers the wide range of these coefficients with both a_m and b_m increasing with Ri, and it has graupel properties as Ri approaches 1. Note that the observed a_m and b_m do not show a consistent increase with Ri due to the various types of rimed particles and graupel observed (Fig. 2b). Temperature and riming intensity dependent a_m and b_m in the scheme cannot fully capture the observed wide range of variation of rimed particles and graupel properties.

Figure 2c shows the variation of derived a_v and b_v with temperature and Ri, which matches relatively well the empirical parameters derived from observations (Locatelli and Hobbs 1974; Mitchell et al. 1990; Mitchell 1996; Barthazy and Schefold 2006), with an increase of both a_v and b_v with Ri. It also indicates that quite different fall speed formulations are used for graupel (circles) and snow (double circles) in BMPs. In contrast to the large impact of Ri on fall speed parameters a_v and b_v, the temperature impact on these parameters is relatively small (Fig. 2d). Recently, Barthazy and Schefold (2006) investigated the fall velocity of graupel and snowflakes of differing riming intensity and different crystal types using observations of particle size, shape, and fall velocity during two winter seasons in the Swiss Alps. They found that the fall velocity of snow depends on both the riming intensity and their crystal type composition. This supports the temperature and Ri-dependent fall speed formulation proposed in this paper. Both a_v and b_v in the *V-D* relationship in their study (their Table 3) increase with the riming intensity, with b_v ranging from 0.2 to 0.4. The a_v and b_v derived in our new BMP scheme also increase with riming intensity (Fig. 2c) and generally range from 0.2 to 0.5 for partially rimed particles. Using snow crystal habit types and the degree of riming measured during two winters

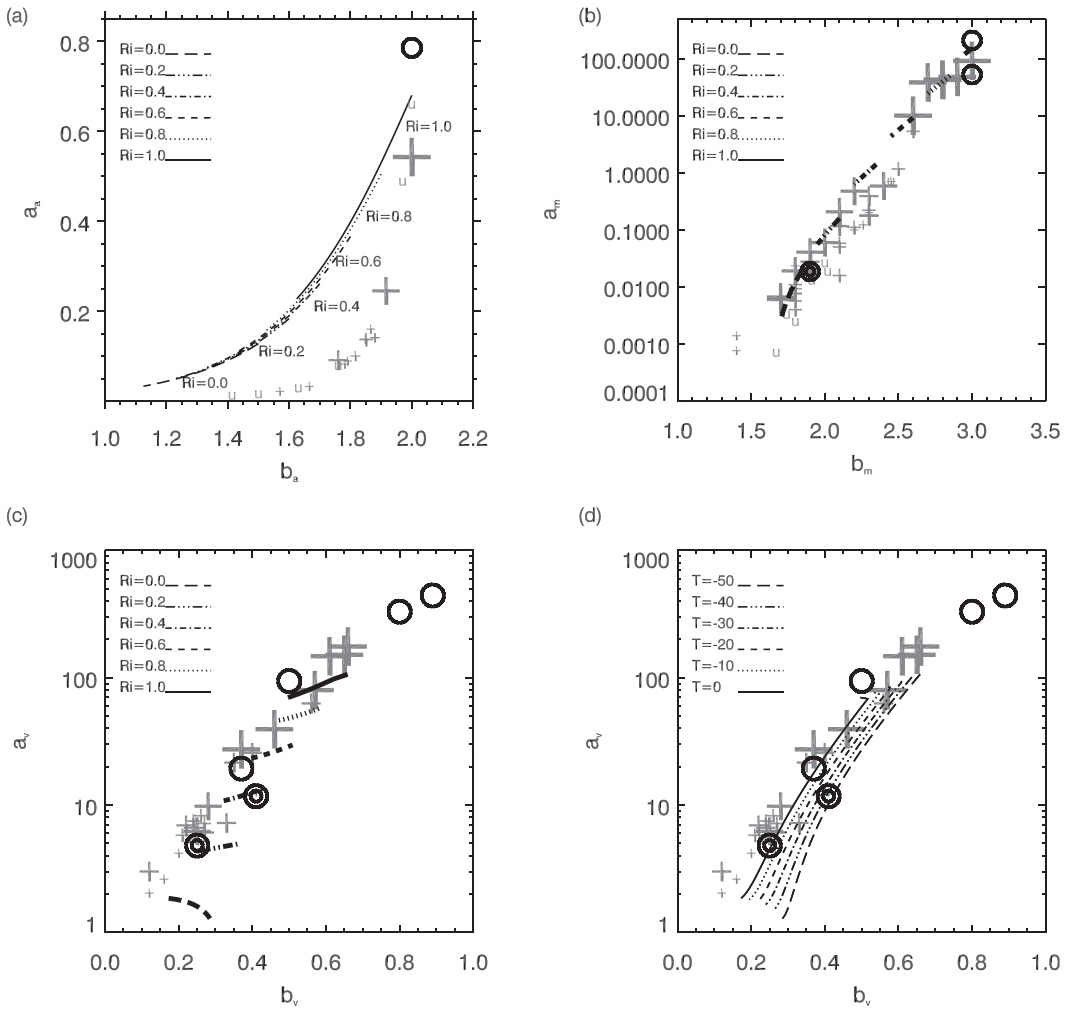

FIG. 2. (a) Coefficients for the area–diameter (*A-D*) relationship in the new scheme for a range of temperatures (−50° to 0°C) and Ri (each line represents the change with temperature for each Ri). The black circle is for spherical particle. Gray crosses (with increasing sizes for increasing riming intensity and *u* for unknown riming intensity) in the figure are the empirical coefficients derived from observations in Locatelli and Hobbs (1974), Mitchell et al. (1990), Mitchell (1996), and Barthazy and Schefold (2006). (b) As in (a), but for the mass–diameter (*M-D*) relationship. Two black circles represent spherical particles with constant density (400 and 100 kg m^{-3} for graupel and snow, respectively) as used in many BMPs. The double black circle represents the Brown and Francis (1995) relationship. (c) As in (a), but for the velocity–diameter (*V-D*) relationship. The four black circles represent *V-D* relationships for graupel used in various WRF BMPs. The two black double circles represent *V-D* relationships of snow in WRF BMPs. (d) As in (c), but each line shows the variation with Ri instead of temperature.

over the Washington Cascade Mountains, Stoelinga et al. (2008) found a similar variation of fall velocity with degree of riming. However, more observations and theoretical studies are needed to better quantify the Ri effect on ice particle properties.

To illustrate the relative impact of Ri and temperature on *M-D* and *V-D*, Fig. 3 shows the empirical *M-D* and *V-D* for different BMPs and ice habits and those predicted in the new scheme. Both mass and velocity of PI in the new scheme increase with Ri and cover a wide range encompassed by those *M-D* and *V-D* relationships used in conventional BMPs (Figs. 3a,b). For example, the *M-D* in the new scheme approaches Thompson et al. (2008) (whose scheme is hereafter referred to as THOM2) for a Ri of ~0.1 and matches Thompson et al.'s (2004) (this scheme is hereafter referred to THOM1) *M-D* as Ri increases to ~0.3. When Ri approaches 1, the new scheme has an *M-D* relation close to the graupel *M-D* value used in THOM1. There is some temperature impact on the *M-D* and *V-D* relationships (Figs. 3c,d), but the variations are smaller than the different ice habits in the literature (Woods et al. 2007). For example,

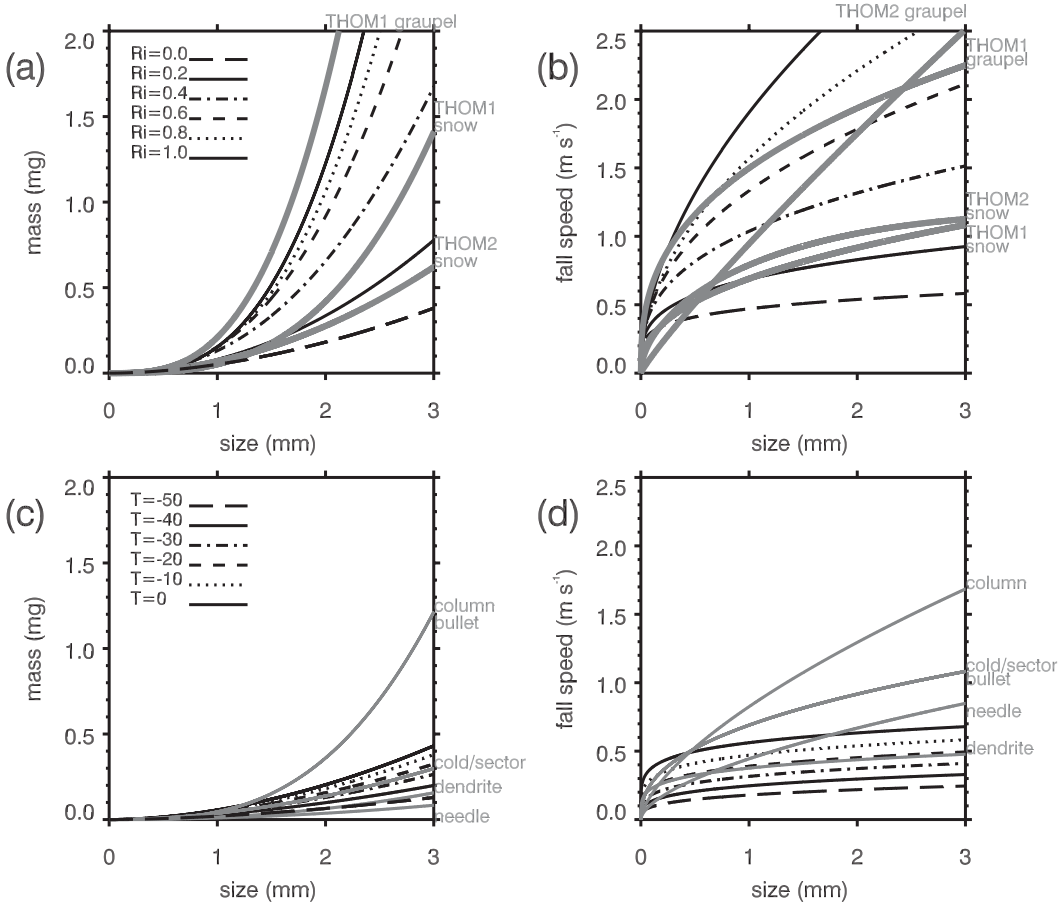

FIG. 3. (a) The *M-D* relationships for various riming intensities (Ri) at −10°C (black lines). The gray lines are the *M-D* relationships used in conventional BMPs. (b) As in (a), but showing the *V-D* relationships for various riming intensities with gray lines representing the *V-D* relationships used in conventional BMPs. (c) The *M-D* relationships for various temperatures and a zero Ri. Gray lines are the *M-D* relationships for different ice habits as summarized in Woods et al. (2007). (d) As in (c), but for the *V-D* relationships.

an observed dendritic ice particle falls relatively slowly (~0.5 m s^{-1}), while a cold-type snow crystal falls much faster (~1.5 m s^{-1}). Thus, most of the changes and potential benefit of this new scheme will be from the Ri impacts. Future work is needed to better include habit impacts on ice particle properties within the scheme.

Ice particle capacitance directly impacts its deposition and sublimation growth and is a function of the size and shape of the ice particle (Rogers and Yau 1989). Westbrook et al. (2008) showed that the capacitance of snow aggregates ($b_m \sim 2$) was only half that of a sphere. Since b_m linearly increases to 3 as Ri increases from 0 to 1, for simplicity we assume (where $C_s = 0.25$ for dry snow and maximum C is 0.5 for spherical particles; Rogers and Yau 1989)

$$C_s = 0.25(1 + \mathrm{Ri}). \quad (14)$$

Following the fact that the exponential distribution gives reasonable estimates of ice water content (Heymsfield et al. 2008b), the conventional exponential size distribution with a temperature-dependent intercept (Houze et al. 1979) is used for PI in the new scheme. Both the *M-D* relationship and intercept parameter in the exponential distribution determine the mass-mean diameter, which is important in all the PI-related microphysical process parameterizations. Woods et al. (2008) compiled and analyzed aircraft measurements between −36° and 0°C over the Oregon coast and Cascades from the IMPROVE project, which include IWC, LWC, temperature, and the intercept and slope parameters by line fitting of measured particle size distribution with a cutoff size of 25 microns. Using observed LWC, IWC, and temperatures, the *M-D* relationships are first computed using the SBU-YLIN approach. Then the inverse of slope parameter (equivalent to the mass-mean diameter multiplied by a b_m-dependent constant) is derived from the observed IWC and the *M-D* relation using

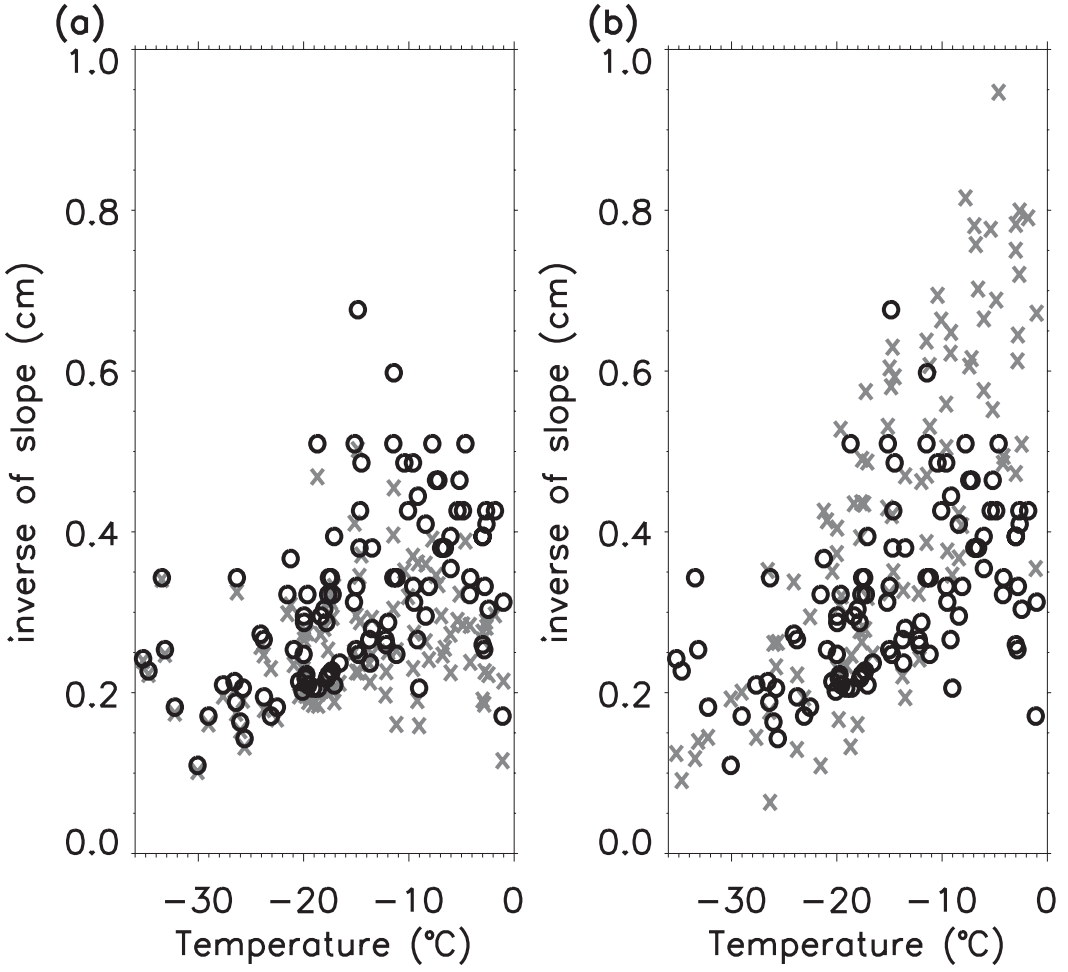

FIG. 4. (a) Observed temperatures (°C) vs the inverse of the slope parameter for snow (cm) from the Convair aircraft measurements (black circles) and that derived from the SBU-YLIN scheme (gray crosses) using the *M-D* relationship derived from the observed LWC, IWC, and temperature. See text for more details. (b) As in (a), but using the temperature-dependent snow intercept (Houze et al. 1979).

$$\lambda^{-1} = \left[\frac{\text{IWC}}{a_m N_0 \Gamma(b_m + 1)}\right]^{1/(b_m+1)}, \qquad (15)$$

where IWC includes small ice particles. Figure 4 shows the observed and predicted inverse of the slope parameters. Observed particle sizes generally increase with increasing temperature from −30° to −10°C as a result of depositional and aggregation growth. Particle sizes decrease as temperature further increases to 0°C. This may be due to the riming and secondary ice generation (Hallett and Mossop 1974) or the shattering of dendrites on the instrument probes (Vidaurre and Hallett 2009). The SBU-YLIN approach depicts well the three dominant ice growth regimes (depositional, aggregation, and riming growth) under different temperatures as observed by aircraft when using the observed intercept (Fig. 4a). In contrast, when the temperature-dependent intercept is used (Houze et al. 1979), particle sizes are too large at temperatures warmer than −10°C and increase with increasing temperature without a transition near −10°C (Fig. 4b). This implies that both realistic *M-D* relationships and intercept parameterization are required to represent realistic ice particle sizes. Future work is needed to better quantify the intercept parameter, such as those used in Thompson et al. (2008) and Boudala and Isaac (2006).

In reality, ice depositional and riming growth can occur concurrently. As cloud liquid droplets accrete to the ice surface and freeze, latent heat is released and the surface temperature of ice particles increases. As a result, the supersaturation over the ice particle surface is reduced and so is the depositional growth (Kong and Yau 1997). The error neglecting the riming

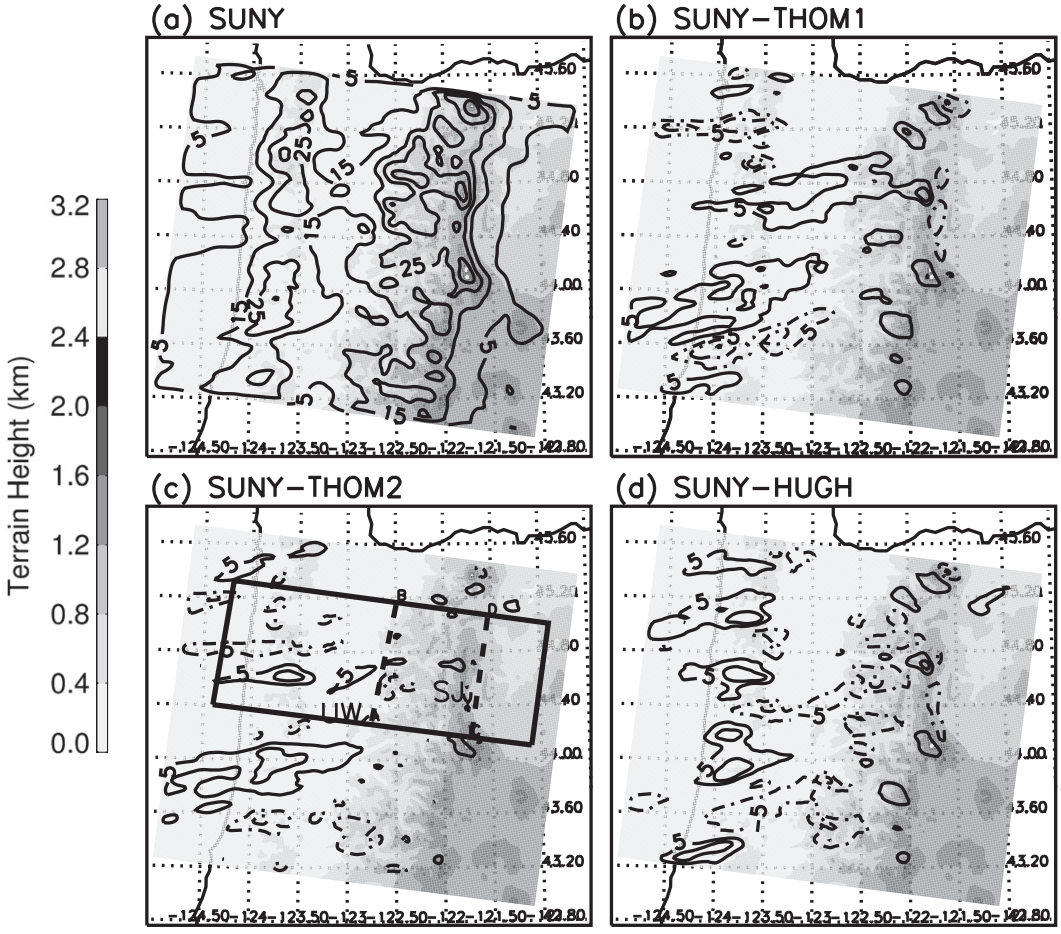

FIG. 5. (a) The 12-h (2000 UTC 4 Dec–0800 UTC 5 Dec) precipitation (mm) from IMPROVE-2 IOP6 for the SBU-YLIN scheme and terrain height (shaded in km). The 12-h precipitation difference (mm) between SBU-YLIN and the (b) THOM1, (c) THOM2, and (d) HUGH schemes. Solid contours (every 5 mm) show where the precipitation is less than SBU-YLIN, while dashed–dotted contours (every 5 mm) indicate where the precipitation is more than SBU-YLIN. The solid line box in (c) shows the region used for the east–west average of microphysics, precipitation, and the water budget in Table 2, while the dashed line box in (c) shows the region to compute the mean vertical profiles of IWC and LWC. UW and SJ respectively denote the location of the University of Washington sounding and the microwave radiometer at Santium Junction.

effect on the depositional growth may be nontrivial. Milbrandt et al. (2010) showed that adding the latent heat effect in the snow depositional growth reduced the snow amount at lower levels where accretion is appreciable. The new scheme adds the riming growth effect on the PI depositional growth parameterization [Eq. (A3) in the appendix]. Other parameterizations related to PI use the new *A-D*, *M-D*, and *V-D* relations.

c. Other modifications

In addition to the new PI parameterizations described above, other modifications in the scheme are briefly presented here. This new scheme uses a generalized gamma distribution to describe the size distribution of cloud water droplets (Liu and Daum 2004):

$$N_c = N_{0c} D^{\mu} e^{-\lambda D}, \tag{16}$$

where N_{0c} is the intercept, μ is the shape parameter, and λ is the slope. The total number concentration of cloud droplets generally depends on the ambient aerosol distribution and properties. In the new scheme, the most representative numbers is used for maritime (100 cm^{-3}) and continental air mass (250 cm^{-3}) when aerosol information is not available. Future work will add the aerosol activation and its interaction with cloud microphysics.

The collision and coalescence of cloud droplets to form raindrops has been described as a simple autoconversion

process by utilizing the cloud liquid water content (Kessler 1969). More physically based autoconversion parameterizations (Berry 1968; Berry and Reinhardt 1974; Walko et al. 1995) have been implemented into some new BMPs (Thompson et al. 2004; Thompson et al. 2008; Hong et al. 2004), which consider the cloud droplet number concentration and the spectral shape of the cloud droplet size distribution besides the liquid water content. Liu and Daum (2004) compared various existing autoconversion parameterizations and derived a new Kessler-type parameterization that suggests a strong dependence of the autoconversion rate on liquid water content, droplet concentration, and relative dispersion (defined as the ratio of the standard deviation to the mean radius of the cloud droplet size distribution). Li et al. (2008) showed that the Liu and Daum formula gave reasonable results for a convective event compared with other autoconversion parameterizations. More specifically, we use Eq. (6) from Liu and Daum (2004) with a critical radius of 10 microns and a number concentration of 100 cm^{-3} in the following preliminary tests. See the appendix for more details. Rain and its related parameterizations are similar to Lin et al. (1983).

The division between cloud ice and PI in the BMP is not as physically based as the division between cloud droplets and rain, which grow by condensation and by collision and coalescence, respectively. Based on aircraft observations, Heymsfield et al. (2007) found that the spherical assumption is good for ice particles with diameters smaller than 90 microns. For these small ice particles, a constant ice density (910 kg m^{-3}) is considered a reasonable approximation given previous studies (Pruppacher and Klett 1997). It is known that small ice crystals under a threshold size (100 microns for plates and about 50 microns for columnar crystals) are unable to collect cloud droplets (Pruppacher and Klett 1997). Thus, a maximum size of 100 microns is applied for cloud ice to snow conversion in the scheme. To simplify the description of ice in BMPs, a monodisperse distribution is widely used (Hong et al. 2004; Thompson et al. 2004), which is also applied here. We also adopted the ice fall speed proposed by Heymsfield and Donner (1990) as used in Hong et al. (2004) for cloud ice.

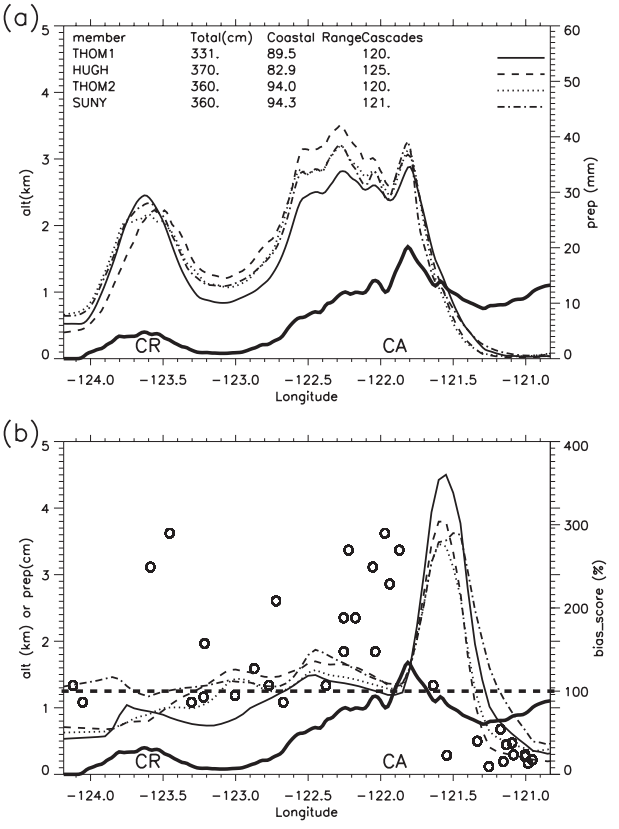

FIG. 6. (a) Simulated WRF precipitation (mm, using the right *y* axis) meridionally averaged across the solid boxed region in Fig. 5c from 2000 UTC 4 Dec to 0800 UTC 5 Dec 2001. The average terrain profile (km) is also indicated using the left *y* axis. (b) The percent of observed precipitation (right *y* axis on plot) at the precipitation gauge sites is shown for the boxed area for the four BMPs. See Colle et al. (2008) for gauge locations and Lin and Colle (2009) for more details about the percent of observed precipitation profile. The circles are the observed 12-h precipitation (cm) at precipitation gauges using the left *y* axis. The thick dashed line denotes 100% of the observed precipitation.

3. IMPROVE-2 comparison

The IMPROVE-2 project in December 2001 collected a comprehensive set of measurements from a variety of remote and in situ instruments over the central Oregon Cascades (Stoelinga et al. 2003). The wealth of observations provides an unprecedented opportunity to rigorously test various BMP schemes (Garvert et al. 2005a,b; Colle et al. 2005; Lin and Colle 2009; Milbrandt et al. 2008, 2010). For example, Lin and Colle (2009) found large sensitivity of surface precipitation and microphysics aloft simulated by different BMPs in the WRF model for an orographic precipitation event during IMPROVE-2. The new SBU-YLIN scheme was implemented in WRF and tested for two well-documented IMPROVE-2 cases [4–5 and 13–14 December 2001, hereafter referred to as intensive observing periods 6 and 9 (IOP6 and IOP9)]. Large liquid water content for IOP9 favored more riming growth and more rapid precipitation fallout. Significant snow overprediction aloft has been documented for these events using different BMPs (Garvert et al. 2005b; Colle et al. 2005; Milbrandt et al. 2008; Lin and Colle 2009). It should be noted that the derived parameters in section 2 were not modified using the data from these two

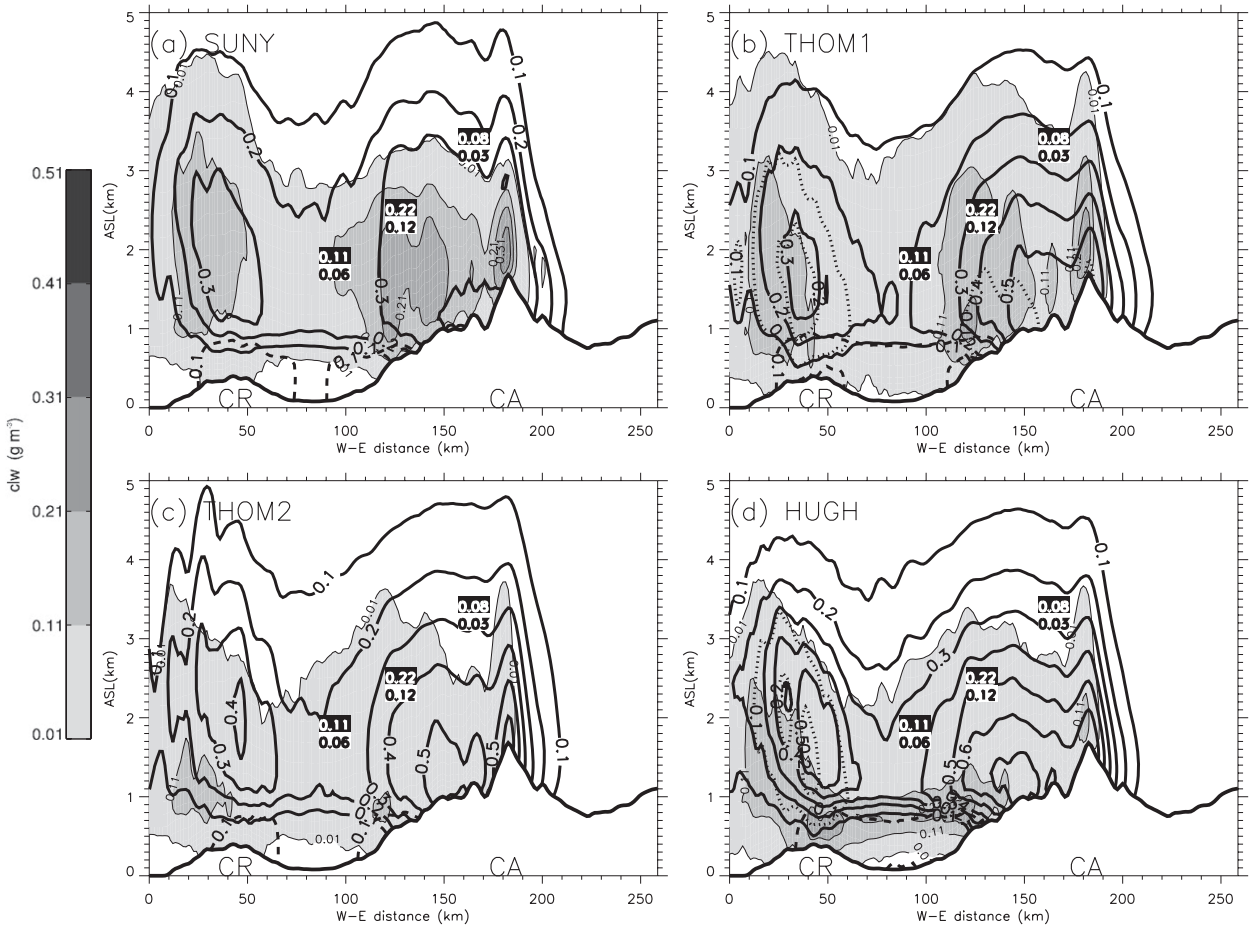

FIG. 7. A west–east cross section across the solid line box in Fig. 5c showing north–south averaged LWC (shaded every 0.1 g m^{-3}), IWC (the sum of snow, graupel, and ice; black solid, every 0.1 g m^{-3}), graupel (black dotted, every 0.1 g m^{-3}), and rain (black dashed, every 0.1 g m^{-3}) for the (a) SBU-YLIN, (b) THOM1, (c) THOM2, and (d) HUGH schemes. The simulated fields were temporally averaged from 2300 UTC 3 Dec to 0200 UTC 5 Dec 2001 (forecast hours 11–14) using the 15-min model output. The boxed numbers are the NOAA P-3 measured IWC (black) and LWC (white) during the same period for each north–south flight leg within the box.

IMPROVE-2 cases, so IMPROVE-2 serves as an independent comparison dataset for the scheme.

a. Experimental setup

The WRF setup and configuration for IOP6 (4–5 December) is identical to Lin and Colle (2009), except that the new SBU-YLIN microphysics scheme is used. For the 13–14 December 2001 case (IOP9), the WRF configuration follows Hahn and Mass (2009). WRF version 2.2 is used for both IOPs, with 1.33-, 4-, and 12-km domains with 32 vertical levels nested within an outer 36-km domain that extends from the central Pacific to the intermountain western U.S. Global Forecast System (GFS) analyses every 12 h were used for the lateral boundary conditions for the full 36-h simulation and the initialization at 1200 UTC 4 December 2001 for IOP6 and 0000 UTC 13 December 2001 for IOP9. Four-dimensional data assimilation (FDDA or analysis nudging; Stauffer and Seaman 1990) was used during the first 24 h in the 36- and 12-km domains, and then it was turned off gradually during the subsequent 6-h period. The physics used for IOP9 include the modified Kain–Fritsch scheme (Kain and Fritsch 1993; Kain 2004) in the 36- and 12-km domains and the medium-range forecast (MRF) planetary boundary layer (PBL) scheme (Hong and Pan 1996). The SBU-YLIN scheme was compared with three other BMPs available in the WRF, which include an older version of Thompson (i.e., THOM1; Thompson et al. 2004), new Thompson (THOM2; Thompson et al. 2008), and a six-category double-moment scheme wherein both the number concentration and mixing ratio are predicted as described in Morrison et al. (2005, 2009), which is hereafter called HUGH). We used the updated version of THOM2 and HUGH as released

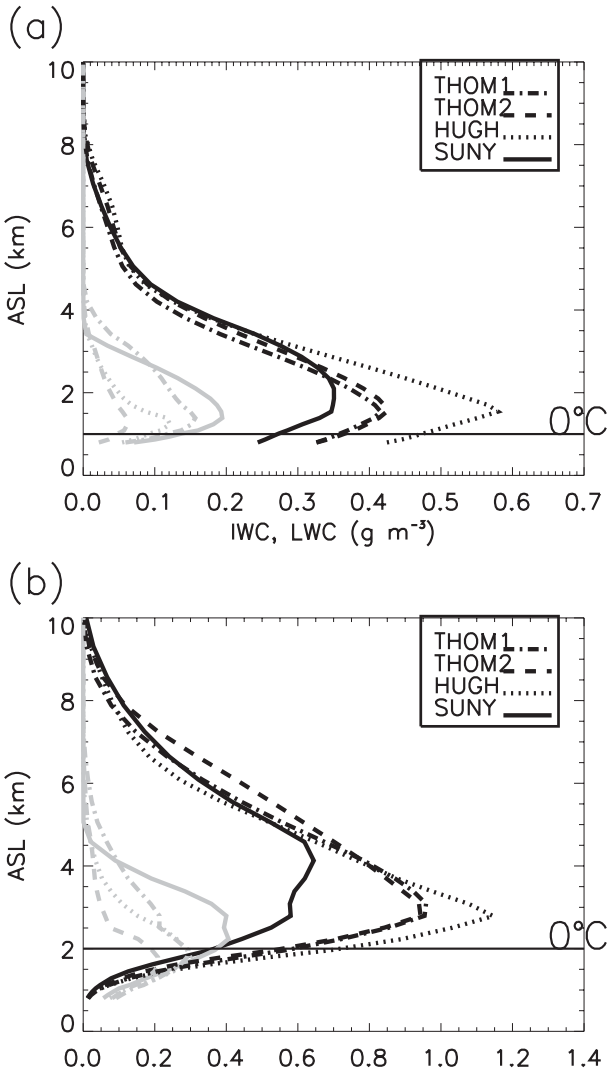

FIG. 8. (a) IWC (black) and LWC (gray) profiles for IOP6 averaged over the Cascades windward slopes and crest (dashed line box in Fig. 5c) using 15-min model outputs from a 3-h period (2300 UTC 4 Dec–0200 UTC 5 Dec) for the four schemes. The freezing level is also indicated. (b) As in (a), but for the mean profiles from a 3-h period (2300 UTC 13 Dec–0200 UTC 14 Dec) for IOP9. The thin lines are IWC (black) and LWC (gray) for the FIXVD (solid) and FIXSC (dashed) runs, respectively.

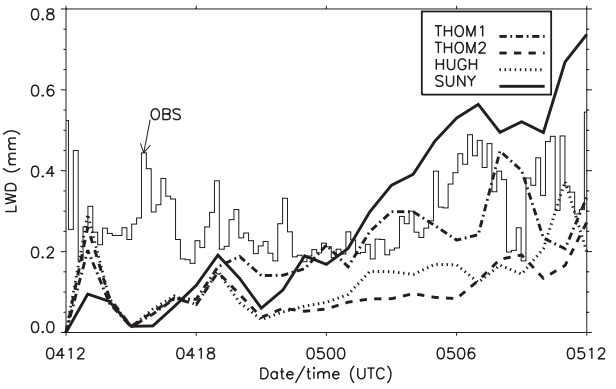

FIG. 9. Vertically integrated liquid water depth (LWD, mm) from the microwave radiometer at Santium Junction (SJ on Fig. 5c) and the four microphysical simulations (THOM1, THOM2, HUGH, and SBU-YLIN) from 1200 UTC 4 to 1200 UTC 5 Dec 2001.

in WRF version 3.1. This helps compare our new scheme with more sophisticated and recently updated schemes in WRF. The Purdue–Lin scheme and WSM6 are not compared because of their dominance by graupel aloft for IOP6 (Lin and Colle 2009). All simulations used the positive definite advective (PDA) scheme for the moisture and hydrometeor advection (Skamarock 2006). The following analysis will present results from the 1.33-km WRF domain.

As highlighted in Colle et al. (2008), the IOP6 event featured a landfalling baroclinic trough over the Pacific Northwest with a relatively low freezing level (~1 km MSL) and embedded convective cells. A detailed description of kinematic and precipitation evolution of the event as well as the WRF model accuracy is presented in Colle et al. (2008) and Lin and Colle (2009). Because of the relatively weak cross-barrier flow (10–15 m s^{-1}) at crest level and low freezing level in IOP6, there is little supercooled cloud liquid water, and the riming growth is relatively small. In contrast, IOP9 featured the passage of an intense baroclinic zone with heavy precipitation, strong (25–30 m s^{-1}) cross-barrier flow, and a relatively high freezing level (~2 km MSL) (Garvert et al. 2005a). Since previous modeling studies of IOP9, such as Garvert et al. (2005b) and Colle et al. (2005), used the fifth-generation Pennsylvania State University–National Center for Atmospheric Research (NCAR) Mesoscale Model

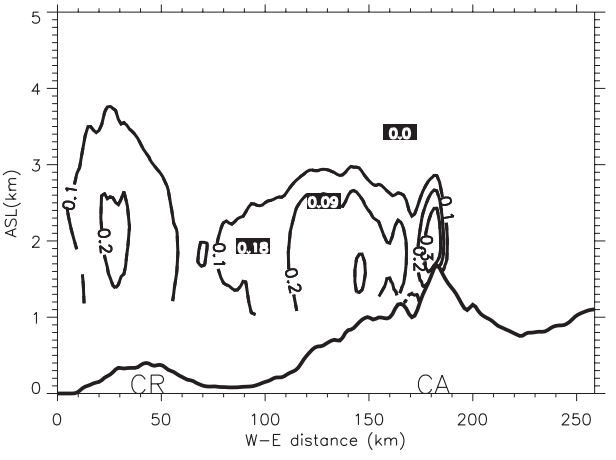

FIG. 10. A west–east cross section showing north–south averaged riming intensity for IOP6 during a 3-h period (2300 UTC 4 Dec–0200 UTC 5 Dec 2001) over the box in Fig. 5c. The black numbers are the Ri estimates from the P-3 measurements (see text for details).

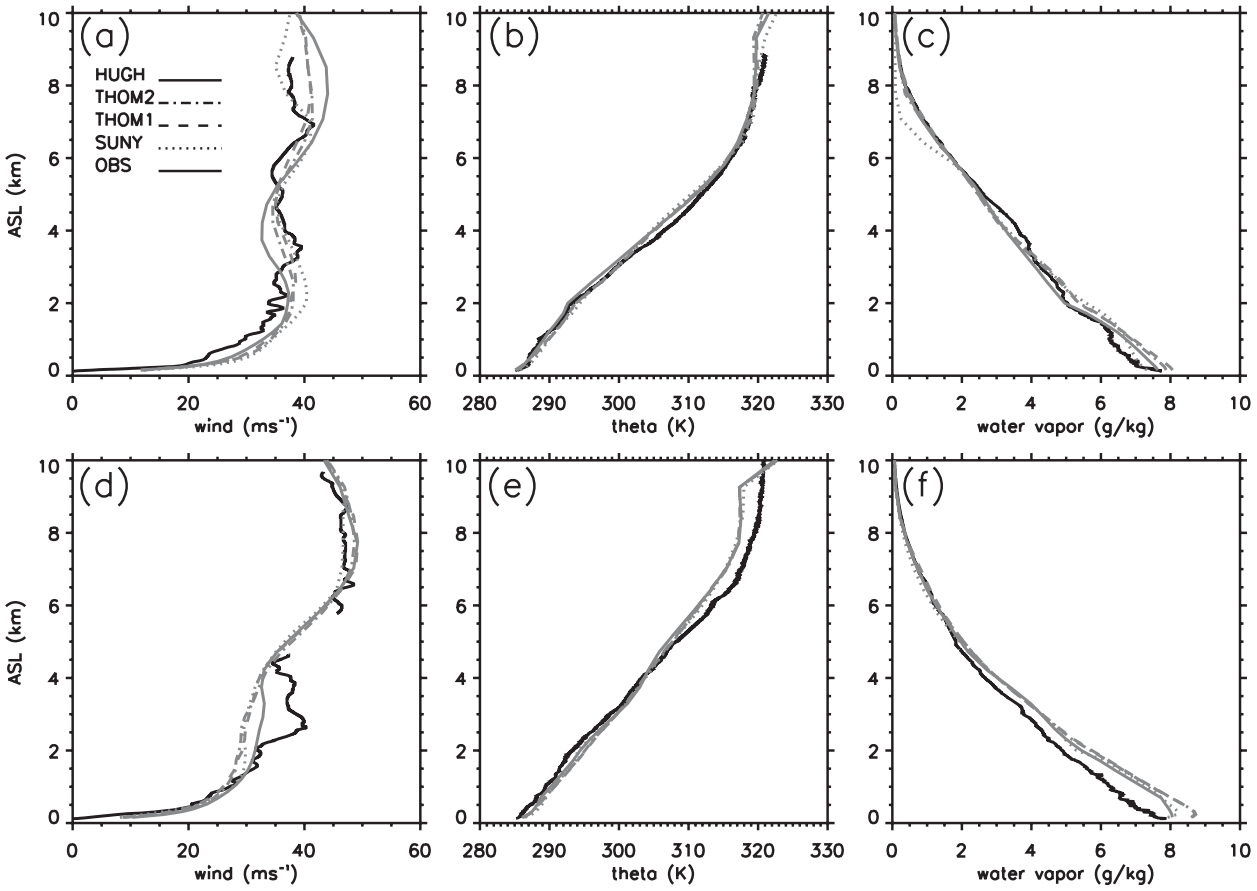

FIG. 11. (a) Vertical profiles of the observed and simulated wind speeds (m s^{-1}) from the four WRF BMP simulations at the UW site at 2100 UTC 13 Dec 2001. (b) As in (a), but for potential temperature (K). (c) As in (a), but for water vapor mixing ratio in (g kg^{-1}). (d)–(f) As in (a)–(c), respectively, but at 0000 UTC 14 Dec 2001.

(MM5; Grell et al. 1994), some evaluation of the ambient conditions in the 1.33-km WRF is presented below for this event.

b. 4–5 December 2001 (IOP6)

The kinematic and thermodynamic evolution for the 4–5 December 2001 event was well simulated using WRF (Lin and Colle 2009). The model winds are a few meters per second weaker than observed (~15 m s^{-1} near crest level), and the simulated potential temperature profile was within 1–2 K of observed (not shown). The general pattern of the 12-h (2000 UTC 4 December–0800 UTC 5 December, or forecast hours 8–20) precipitation distribution in the SBU-YLIN scheme is similar to the other BMPs, with heavy (2–5 cm) precipitation over the Oregon Coastal Range and Cascades, 0.5–1.5 cm in the Willamette Valley, and an obvious rain shadow in the lee of the Cascades (Fig. 5a). The SBU-YLIN scheme produces 0.5–1.0 cm (10%–20%) more precipitation over parts of the Coastal Range than other three schemes, especially over the southern part of the Coastal Range. There is also 0.5–1.0 cm more precipitation over some windward ridges and crest of the Cascades in the SBU-YLIN scheme as compared to the other schemes. The new scheme slightly reduces the precipitation spillover over the Cascade crest, with ~0.2 cm less precipitation in the immediate lee than in THOM1 (Fig. 5b). The precipitation difference between SBU-YLIN and THOM2 is rather small over the Cascades (Fig. 5c). SBU-YLIN predicts ~20% more precipitation over the Coastal Range and 10%–20% less precipitation over the windward Cascades than the HUGH scheme (Fig. 5d). Figure 6a shows an east–west profile of north–south averaged precipitation within a box (see Fig. 5c for location) for the four BMP simulations over the Oregon Coastal Range and Cascades from IOP6 (2000 UTC 4 December–0800 UTC 5 December 2001). Most of the schemes produce similar precipitation amounts over these barriers (within ~10%), while the THOM1 scheme has 10%–20% less precipitation over the Cascades and upstream Willamette Valley than the other schemes. Overall, the new scheme produces

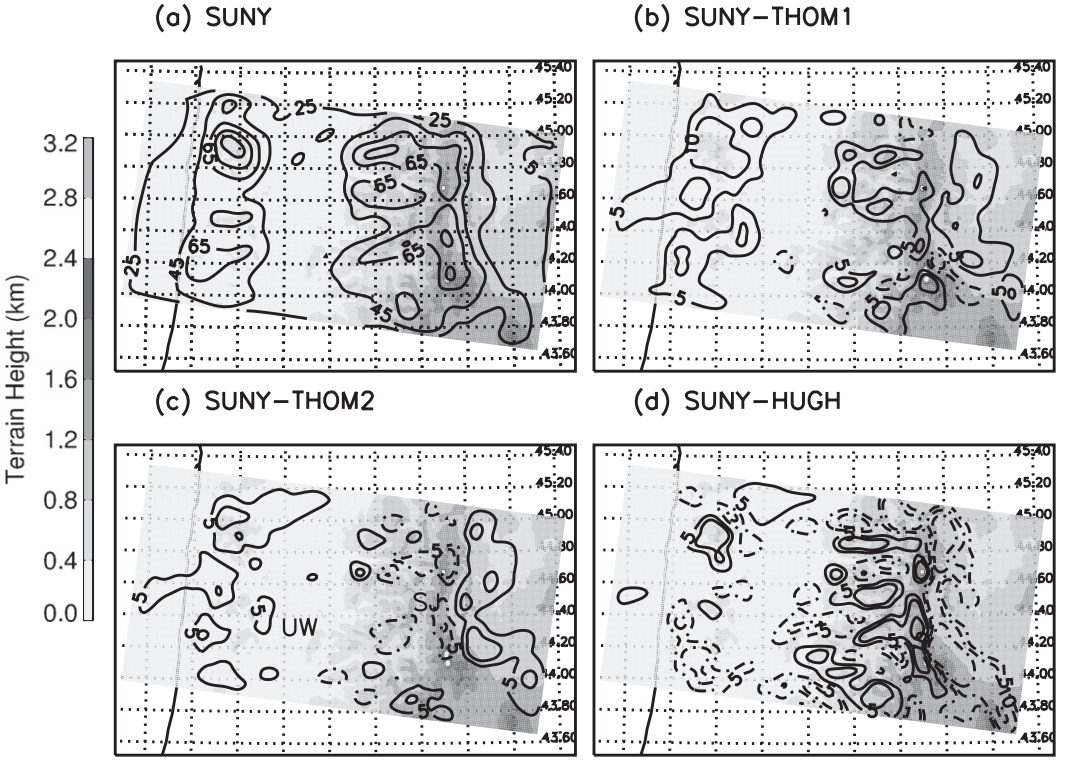

FIG. 12. (a) The 18-h (1400 UTC 13 Dec–0800 UTC 14 Dec; IOP9) precipitation for the SBU-YLIN scheme (contoured every 20 mm); terrain height (km) is shaded for reference. The 18-h precipitation difference (mm) between SBU-YLIN and the (b) THOM1, (c) THOM2, and (d) HUGH schemes. The solid contours illustrate areas where the precipitation is less than SBU-YLIN, while dashed–dotted contours indicate areas with more precipitation than SBU-YLIN.

precipitation amounts comparable to many other WRF schemes for this case.

The surface gauge precipitation and the model percent of observed precipitation are illustrated using the stations averaged meridionally within the box and plotted from west to east (Fig. 6b). Compared with ~30% underprediction by other schemes over the Coastal Range, the SBU-YLIN scheme predicts precipitation within 20% of the observed from the Coastal Range to the windward slopes and crest of the Cascades. There is dramatic overprediction in the immediate lee for all schemes, which is slightly less for THOM2. The overprediction in the lee has some uncertainty, since there were only two rain gauges and the possibility existed of gauge undercatchment of frozen precipitation. Overall, the mean absolute error (MAE) is similar (~0.5 cm) among the schemes.

A west–east cross section of hydrometeors meridionally averaged over the black box in Fig. 5c was constructed for the four WRF BMP schemes (Fig. 7). Observed IWC and LWC are from the averaged in situ measurements of north–south National Oceanic and Atmospheric Administration (NOAA) P-3 flight tracks within this same box (Lin and Colle 2009). IWC retrieved from P-3 measurements during IOP6 has a 20%–40% uncertainty depending on altitude (Lin and Colle 2009). The SBU-YLIN and THOM1 predict larger (~0.1 g m^{-3}) LWC over the Cascades than do the THOM2 and HUGH schemes, with the SBU-YLIN and THOM1 comparing better (within 20%) with the P-3 observations. The IWC structures among the schemes are similar over the Coastal Range and Cascades, with 0.05–0.25 g m^{-3} overprediction in all schemes over the Cascades. The HUGH scheme predicts ~0.1 g m^{-3} more IWC than the other three BMPs, while SBU-YLIN produces 0.2–0.3 g m^{-3} (30%–50%) less IWC than THOM2 and HUGH over the Cascades at 1.5–3.5 km MSL and thus compares better with the P-3 measurements.

Another view of the IWC and LWC for the various BMPs is shown in Fig. 8a, which shows the mean vertical profiles of IWC and LWC over the Cascade windward slopes (dashed line box in Fig. 5c). Maximum IWC is near 1.6 km MSL (approximately −4°C) for HUGH, THOM1, and THOM2, with ~0.58 g m^{-3} for HUGH and 0.43 g m^{-3} for THOM1 and THOM2. SBU-YLIN has a smaller maximum IWC (~0.35 g m^{-3}) in a layer

between 1.5 and 2.5 km MSL. SBU-YLIN and THOM1 have 2–3 times larger LWC than HUGH and THOM2 below 3 km MSL. Above 3.5 km MSL, where there is little LWC, the various schemes predict more similar IWC, thus emphasizing that most of the differences are in lower mixed phase regions of the cloud.

Liquid water depth (LWD) measured by the radiometer at Santium Junction (labeled SJ in Fig. 5c) at 1.1 MSL provides another check of the cloud water prediction (Fig. 9). LWD gradually increases from 0.2 to 0.5 mm from 0000 to 0700 UTC 5 December before the passage of a midlevel trough. LWD decreases to 0.18 mm with the passage of surface trough at 0900 UTC 5 December and rebounds to ~0.4 mm with the postfrontal convection. Consistent with Fig. 8a, SBU-YLIN and THOM1 predict larger LWD than HUGH and THOM2, with THOM1 and SBU-YLIN LWD predictions slightly less and greater than the observations after 0000 UTC 5 December, respectively. Compared with radiometer observations, HUGH and THOM2 significantly underpredict the LWD by ~70%. LWC underprediction in THOM2 and HUGH over the Cascades limits the riming growth and thus there is negligible graupel aloft (Figs. 7c,d).

In situ measurements from aircraft also provide an estimate of graupel (including partially rimed crystals) mass and total IWC (Woods et al. 2005). This gives a useful estimate of Ri from observations, which is the ratio of the graupel and total IWC estimates from aircraft (Woods et al. 2005). However, this observed Ri is uncertain and quantitative comparison with model results should be taken with caution. Figure 10 shows the west–east cross section of meridionally averaged Ri from the SBU-YLIN run overlaid with the Ri estimated from the P-3. The SBU-YLIN run predicts maximum Ri up to 0.2 over the Coastal Range and ~0.3 over the windward slopes and crest of the Cascades (Fig. 10). These values are generally within 0.1 of Ri estimated from aircraft. In contrast, the THOM2 and HUGH schemes had very little graupel (riming) aloft (<5% of IWC), while THOM1 had ~20% of the IWC as graupel over the Cascades windward slopes. Overall, these results suggest that the Ri parameterization and new PI approach in the SBU-YLIN scheme realistically capture the riming variability. The IWC differences are relatively small between the schemes for this IOP, since riming was relatively light; thus, the 13–14 December event was also verified, since it had more riming.

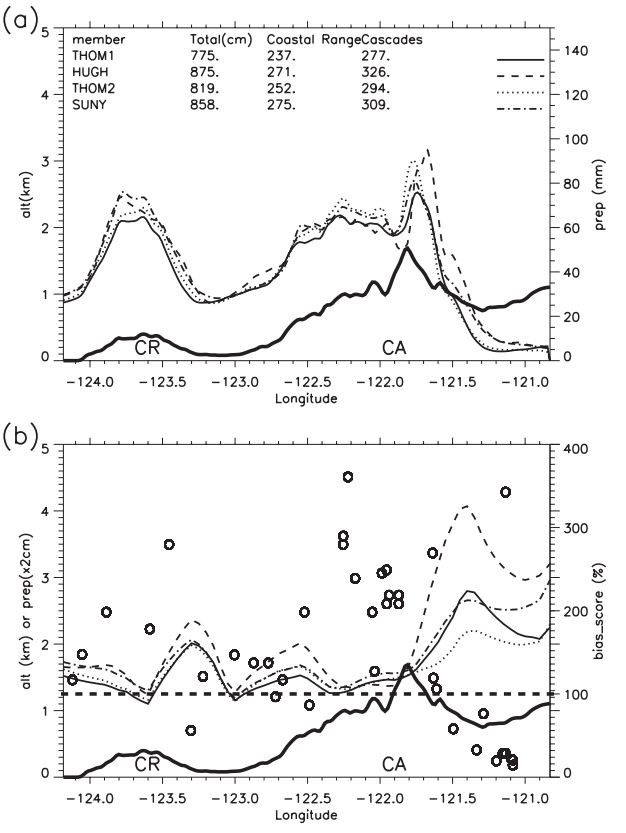

FIG. 13. As in Fig. 6, but for 1400 UTC 13 Dec–0800 UTC 14 Dec 2001 (IOP9).

c. 13–14 December 2001 (IOP9)

Garvert et al. (2005a,b, 2007) extensively evaluated the MM5 simulations for the 13–14 December event (IOP9) in terms of the large-scale forcing, kinematic, thermodynamic, and precipitation evolution. The WRF simulations in our study used the same initial and boundary conditions as the MM5 and similar physics packages, but the model upstream temperature, moisture, and winds were still verified before evaluating the precipitation and microphysics aloft. Figure 11 shows the observed and model wind speed, potential temperature, and moisture at 2100 and 0000 UTC 13 and 14 December at UW (see UW in Fig. 5c). Before the period of heavy precipitation, cross-barrier flow up to 35 m s^{-1} at 1–2 km MSL, temperature, and moisture upstream of the Cascades are well simulated (Figs. 11a–c). However, during the stratiform precipitation period at 0000 UTC 14 December (Fig. 11d), the simulated cross-barrier flow between 2 and 4 km MSL is ~8 m s^{-1} too weak, as noted in previous studies (Garvert et al. 2007; Milbrandt et al. 2008). Simulated profiles are slightly too warm and moist from the surface up to 4 km MSL at this time as well (Figs. 11e,f). The wind and moisture profiles at UW for the various BMP schemes are close (within ~5%), thus allowing a fair comparison of precipitation and microphysics.

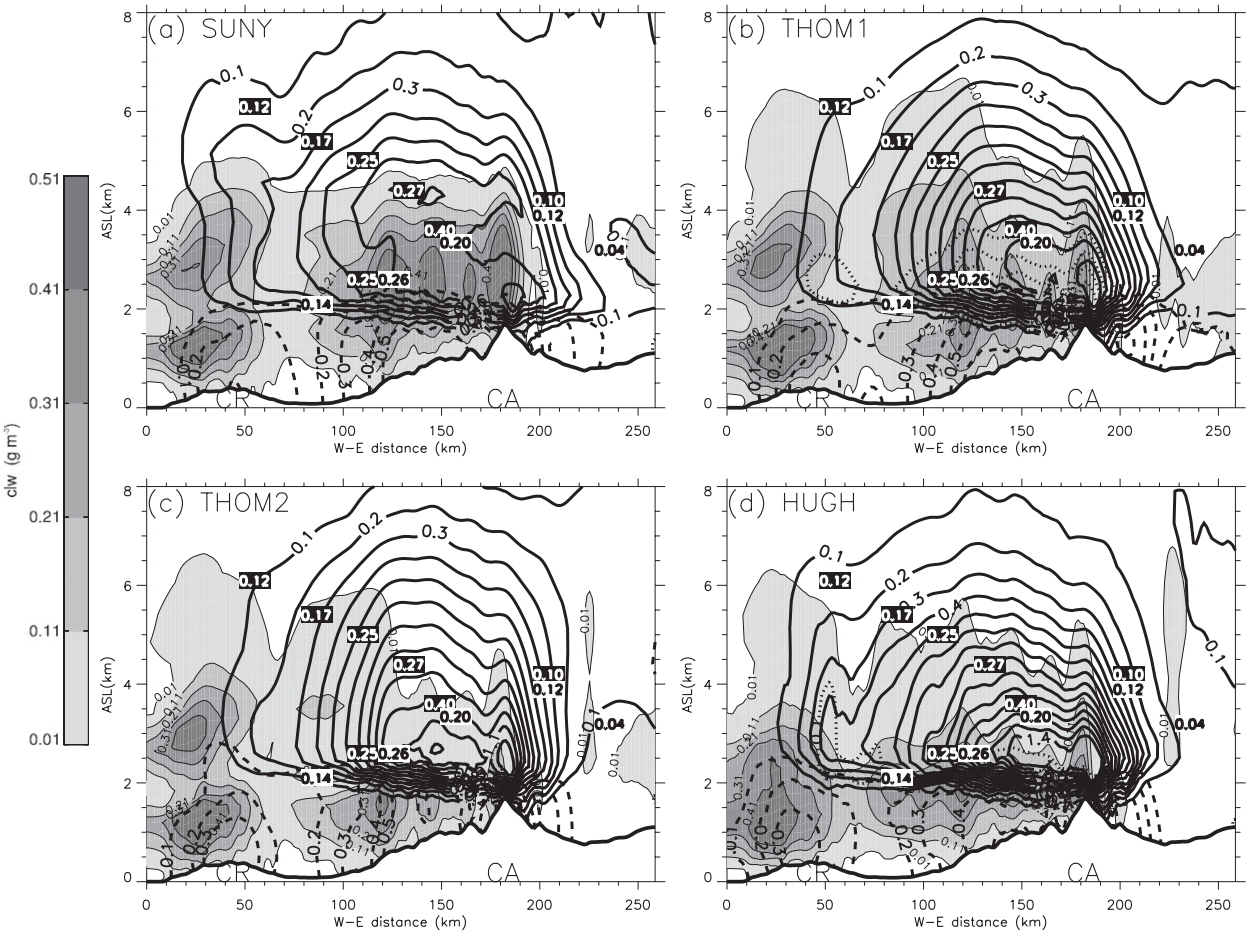

FIG. 14. As in Fig. 7, but for 2300 UTC 13 Dec–0200 UTC 14 Dec 2001 (forecast hours 23–26) of IOP9. The boxed numbers are the Convair measured IWC (white) and NOAA P-3 measured IWC (white) and LWC (black) during the same period.

Like the other BMPs for IOP9, the SBU-YLIN scheme produced two precipitation maxima of 6–8 cm over the Coastal Range and windward slopes of the Oregon Cascades for the 18-h period 1400 UTC 13 December–0800 UTC 14 December 2001 (Fig. 12a). The SBU-YLIN has ~1 cm (15%) more precipitation over the Coastal Range, located farther east of the Cascades, than THOM2 (Fig. 12c). THOM1 predicts 1–2 cm (15%–30%) less precipitation than SBU-YLIN over the Coastal Range and windward slopes of Cascades (Fig. 12b). Meanwhile, the HUGH scheme produces 2–3 cm more precipitation than the SBU-YLIN scheme over the lee of Cascades, while its precipitation over the windward Cascades is 1–2 cm less than the SBU-YLIN run (Fig. 12d).

Figure 13 shows a west–east profile of north–south averaged precipitation for the four BMP simulations over the Oregon Coastal Range and Cascades from 1400 UTC 13 December to 0800 UTC 14 December 2001. The precipitation profiles for the various schemes are similar, with relatively heavy precipitation over the Coastal Range and windward slopes of Cascades, and a rain shadow in the Cascades' lee (Fig. 13a). The total precipitation amounts within the box (in Fig. 5c) for the four schemes are within 15%, with SBU-YLIN and HUGH predicting

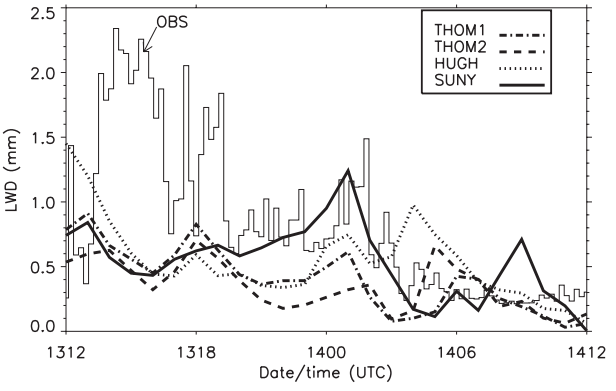

FIG. 15. As in Fig. 9, but for 1200 UTC 13 Dec–1200 UTC 14 Dec 2001 of IOP9.

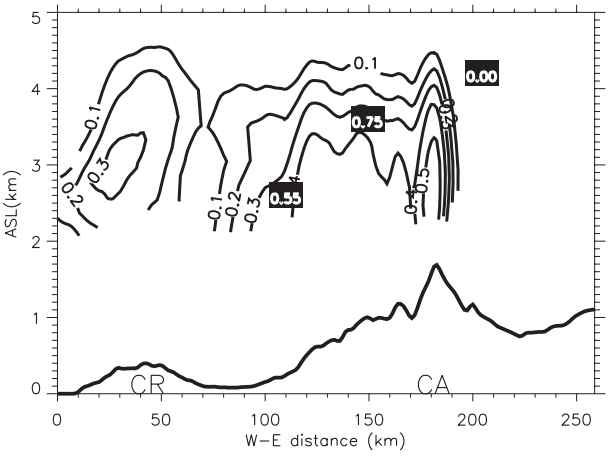

FIG. 16. As in Fig. 10, but for IOP9 during a 3-h period (2300 UTC 13 Dec–0200 UTC 14 Dec 2001).

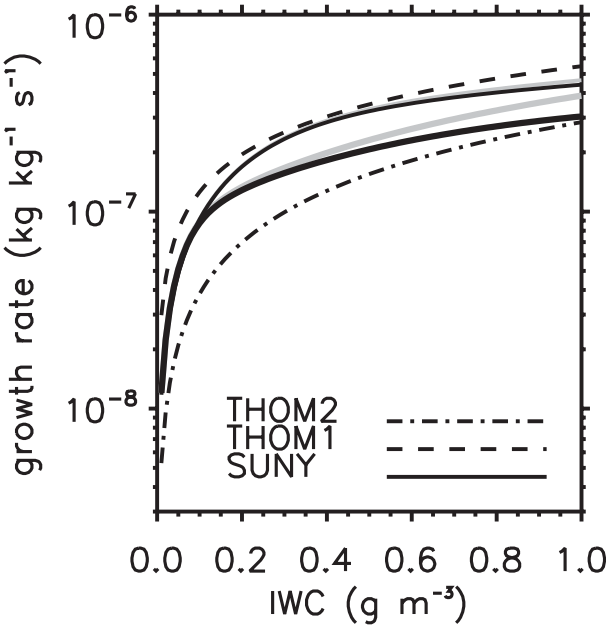

FIG. 17. Parameterized snow depositional growth rates at −15°C from THOM1 (dashed line), THOM2 (dashed–dotted line), and SBU-YLIN [solid lines using LWC of 0.1 (thin) and 0.5 (thick) times of IWC, respectively]. Note that black (gray) solid lines denote the snow depositional growth rate including (excluding) the riming-induced latent heat release.

larger precipitation than THOM2 and THOM1. Most of the difference is over the Cascades, with THOM2 predicting ~20% more precipitation than THOM1. The peak precipitation over the Cascades shifts ~10 km to the east in the HUGH compared with other BMPs.

Figure 13b shows the observed and simulated surface precipitation meridionally averaged and plotted from west to east for the box in Fig. 5c and the model percent of observed precipitation. The precipitation is within 30% of the observed from the Coastal Range to the windward Cascades for the various schemes. However, HUGH gives a larger overprediction than other schemes over the lee of Cascades. Similar to IOP6, all schemes overpredict precipitation in the lee of Cascades, although the overprediction magnitude is smaller than IOP6. Overall, all schemes have similar MAE (~1.2 cm) except HUGH (~1.6 cm) for the precipitation gauges in the model domain.

During IOP9, THOM1, THOM2, and HUGH predict IWC up to 1.2 g m^{-3} over windward slopes and crest of the Cascades at 2.5–3.0 km MSL (Fig. 14). In contrast, SBU-YLIN predicts IWC up to 0.7 g m^{-3} and compares better with the IWC observed by the Convair (0.27 g m^{-3}) and P-3 (0.40 g m^{-3}) aircrafts. The Purdue–Lin scheme and WSM6 predict ~0.4 and 0.7 g m^{-3} of graupel instead (not shown), which is not supported by the aircraft measurements. Consistent with IOP6, HUGH predicts the maximum IWC (~1.15 gm^{-3}) and THOM1 and THOM2 predict similar maximum IWC (~0.95 gm^{-3}) near 3 km MSL (Fig. 8b), whereas maximum IWC predicted by SBU-YLIN is ~0.6 gm^{-3} over a layer from 3 to 5 km MSL over the windward Cascades. Similar to IOP6, LWC is largest for SBU-YLIN and smallest for THOM2 (Fig. 8b). LWC extends to 5 km MSL in the SBU-YLIN, with maximum values up to 0.4 g m^{-3}, while THOM2 and HUGH predict generally less than 0.2 g m^{-3} LWC near the freezing level over the Cascades (Fig. 8b). Compared with aircraft observations, SBU-YLIN slightly overpredicts LWC, while HUGH and THOM2 underpredict LWC. THOM1 predicts up to 0.3 g m^{-3} graupel over the Cascades, while THOM2 produces little graupel (Fig. 14). The rain distribution is similar among four schemes (Fig. 14). Overall, SBU-YLIN reduces the IWC overprediction aloft, as noted in other BMPs for this IOP (Garvert et al. 2005b; Milbrandt et al. 2008).

Figure 15 shows the observed and simulated LWD variations for IOP9. LWD has fairly large values (up to 2.4 mm) from 1300 to 2000 UTC 13 December, while all the runs underpredict the relatively shallow water

TABLE 2. Description of sensitivity experiments. Each experiment is identical to the control simulation except as described here.

Expt name	Description and note
FIXRI	Fixed Ri (0.2) gives smaller *M-D* and *V-D* relation than THOM1 (cf. Fig. 3)
FIXVD	Same *V-D* as in THOM1 to emphasize the importance of fallout
FIXMD	Same *M-D* as in THOM1, *M-D* impact slope parameter and thus all snow processes
FIXSC	Fixed snow capacitance (0.5) to increase the snow depositional growth

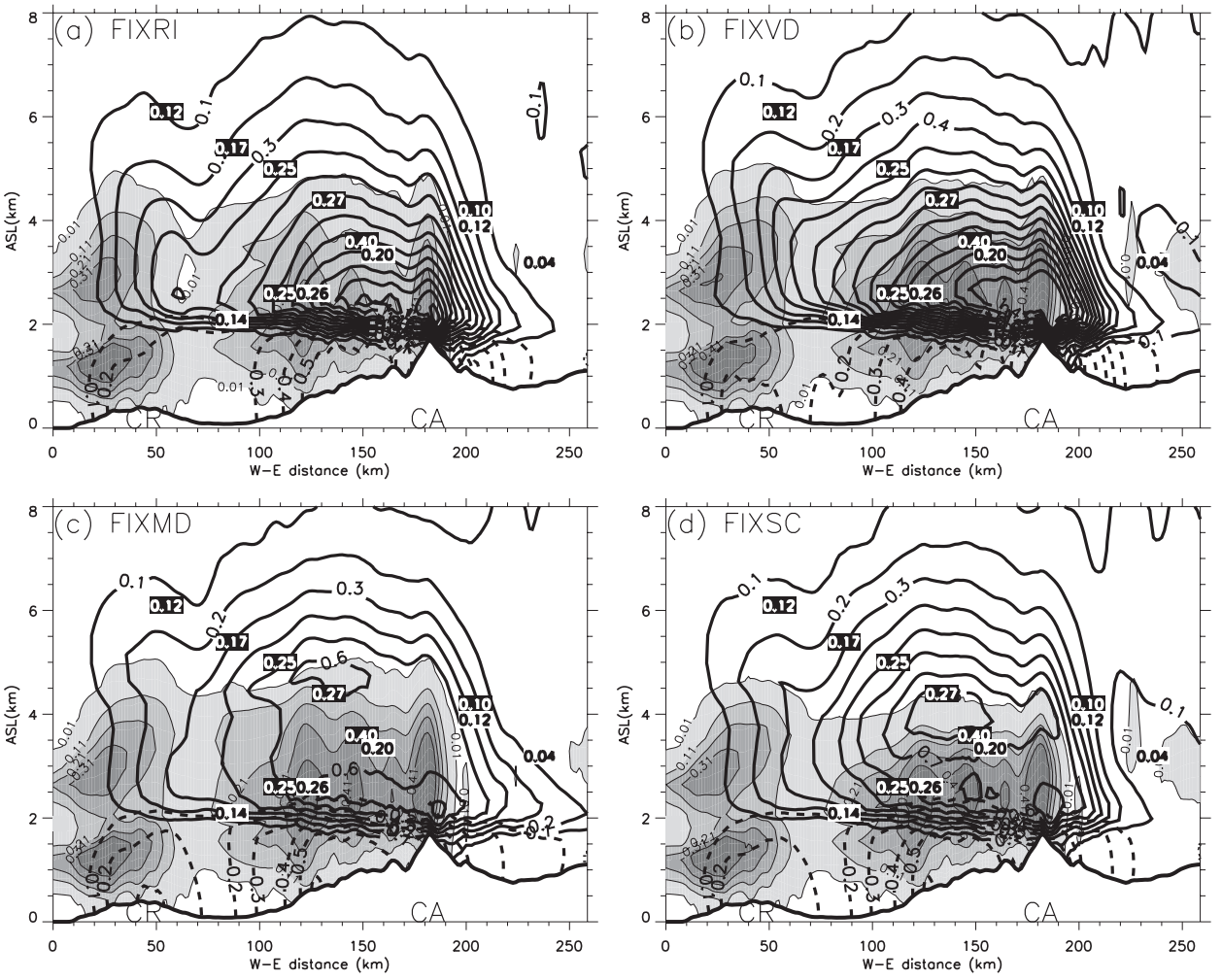

FIG. 18. As in Fig. 14, but showing the (a) fixed Ri run, (b) fixed *V-D* run, (c) fixed *M-D* run, and (d) fixed snow capacitance run. See the text and Table 2 for details.

clouds with little ice aloft (not shown). The LWD increases again to 1.5 mm as the surface front passes at ~0200 UTC 14 December and then drops down to 0.25 mm after frontal passage (Fig. 15). All simulations predict some of the observed LWD variations, but the magnitude is smaller than observed except for SBU-YLIN from 2000 to 0300 UTC. The simulated Ri is up to 0.3 and 0.4 over the Coastal Range and Cascades, respectively (Fig. 16). The model Ri drops quickly to 0 over the lee of Cascades. Compared with P-3 estimates, the SBU-YLIN 3-h mean Ri is somewhat smaller. However, considering the large variation of LWC modeled and thus the large fluctuations of Ri, the model values are within a reasonable range.

d. Discussion

The SBU-YLIN scheme reduces the IWC aloft and has a larger LWC compared with THOM2 and HUGH. The discussion aims to answer why the new scheme reduces the IWC aloft. Snow depositional growth and fallout are the dominant source and sink terms for the IWC aloft in IOP9 (Colle et al. 2005). Figure 17 shows the snow depositional growth rates in THOM1, THOM2, and SBU-YLIN at −15°C assuming saturation with respect to water. Although both THOM1 and SBU-YLIN use the same temperature-dependent intercept, snow depositional growth rate in SBU-YLIN [Eq. (A3)] is ~1–2 times smaller than in THOM1 because of the reduced capacitance given Eq. (14) (THOM1 uses a fixed value of 0.5) and Ri-dependent *M-D* and *V-D* relationships (Fig. 3). Inclusion of latent heat release from riming in Eq. (A3) further reduces the snow deposition rate in SBU-YLIN (Fig. 17). As LWC and Ri increase, snow depositional growth rate in SBU-YLIN decreases and becomes ~2–3 times smaller than in THOM1 for most IWC (Fig. 17). Although THOM2 has a smaller snow

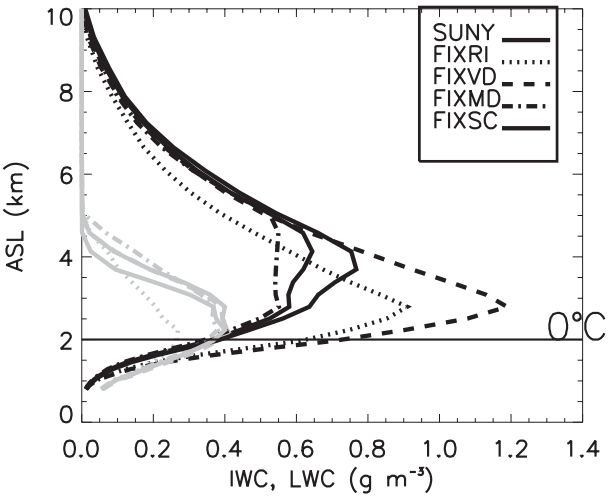

FIG. 19. As in Fig. 8, but showing the IWC and LWC profiles for SBU-YLIN and the four sensitivity runs of IOP9.

depositional rate than SBU-YLIN, the larger IWC aloft for IOP9 may be due to the underestimated LWC and riming in THOM2 (Figs. 14c and 15). Future work will need to investigate why the LWC and riming is less in THOM2.

To investigate the relative impact of various modifications in the SBU-YLIN scheme, four sensitivity tests were conducted to evaluate the relative impact of Ri, *V-D*, *M-D*, and snow capacitance on the IWC aloft, respectively (Table 2). Compared with the control run, using a fixed *V-D* relationship as in THOM1 (the FIXVD scheme) nearly doubles the IWC, with the maximum IWC shifted to a lower level (~2.8 km MSL), and FIXVD has the largest IWC among the various experiments and BMPs (Figs. 18b and 19). Using a fixed Ri = 0.2 yields smaller *M-D* and *V-D* relationships than THOM1 (FIXRI in Table 2). This reduces the IWC by ~20% relative to FIXVD (Figs. 18 and 19), while it increases the IWC relative to the control by 30%–40% at 2–4 km MSL (Fig. 19). FIXRI also reduces LWC by ~30% compared with the control simulation (Figs. 18a and 19). In contrast, the IWC differences between FIXMD (same *M-D* as THOM1 in Fig. 3a; Table 2) and the control, and between FIXSC (same snow capacitance as THOM1, 0.5) and the control, are within 15% (Fig. 19). Compared with the control run, the FIXSC run increases the IWC by 20%–30% near 4 km MSL and depletes LWC there because of increased snow depositional growth (Fig. 18d). Snow depositional growth is inversely proportional to slope parameter [Eq. (A3)] and this implies that the smaller *M-D* relationship favors more snow depositional growth. Compared with FIXMD, the control simulation has a smaller *M-D* and thus larger snow deposition in regions where Ri < 0.3 (cf. Fig. 3), that is, above ~4 km MSL (Fig. 16). As a result, the FIXMD run reduces the IWC aloft (Figs. 18c and 19). Consistent with reduced fall speed of PI in FIXRI and FIXVD run, more PI is advected downwind and contributes to ~80% and 100% more downstream precipitation than the control run and ~15% and 30% less precipitation over the windward slopes (Figs. 20a,b). In contrast, surface precipitation changes only slightly between the FIXSC, FIXMD, and the control runs (Figs. 20c,d). This implies that fallout as influenced by variations of Ri has a larger impact on IWC aloft and surface precipitation than other changes such as snow depositional growth.

To further explore the large (~50%) IWC reduction relative to other BMPs using SBU-YLIN for IOP9, a box water budget following Lin and Colle (2009) was conducted for a 3-h period (2300 UTC 13 December–0200 UTC 14 December) over the box shown in Fig. 5c. The SBU-YLIN scheme has a 2100-s residence time for hydrometeors aloft, which is smaller than HUGH (2300 s), THOM2 (2400 s), and THOM1 (2600 s). Consistent with the relatively short residence time, the SBU-YLIN drying ratio (surface precipitation divided by incoming water vapor flux over the box in Fig. 5c) is 5%–10% larger than the other BMPs (Table 3). The analyses and sensitivity tests suggest that both reduced depositional growth relative to the THOM1 scheme and more efficient fallout in the mixed phase region of the cloud contribute to the significant reduction of IWC aloft in SBU-YLIN.

4. Summary and conclusions

A new approach for representing the ice microphysics is presented, which considers both temperature and riming effects on ice properties. In contrast to traditional BMPs, the graupel category is included in the precipitating ice category through the introduction of a varying riming intensity parameter. The new scheme (SBU-YLIN) allows for physically based representation of the ice particles with temperature- and riming intensity–dependent properties, such as the mass, cross-sectional area, and fall velocity relationships. Riming intensity is diagnosed from LWC, precipitating ice (PI) mass, and temperature. One advantage of the new approach is the simplification of the scheme and the reduction of the computation time. Also, it is more physically based than many existing schemes, since it considers partially rimed particles.

Preliminary tests of the new scheme using data from the IMPROVE-2 project over the central Oregon Cascades suggests that the new approach using riming intensity (Ri) and a continuous snow to graupel category is promising. For both IMPROVE-2 cases, surface precipitation and microphysics aloft using the new scheme

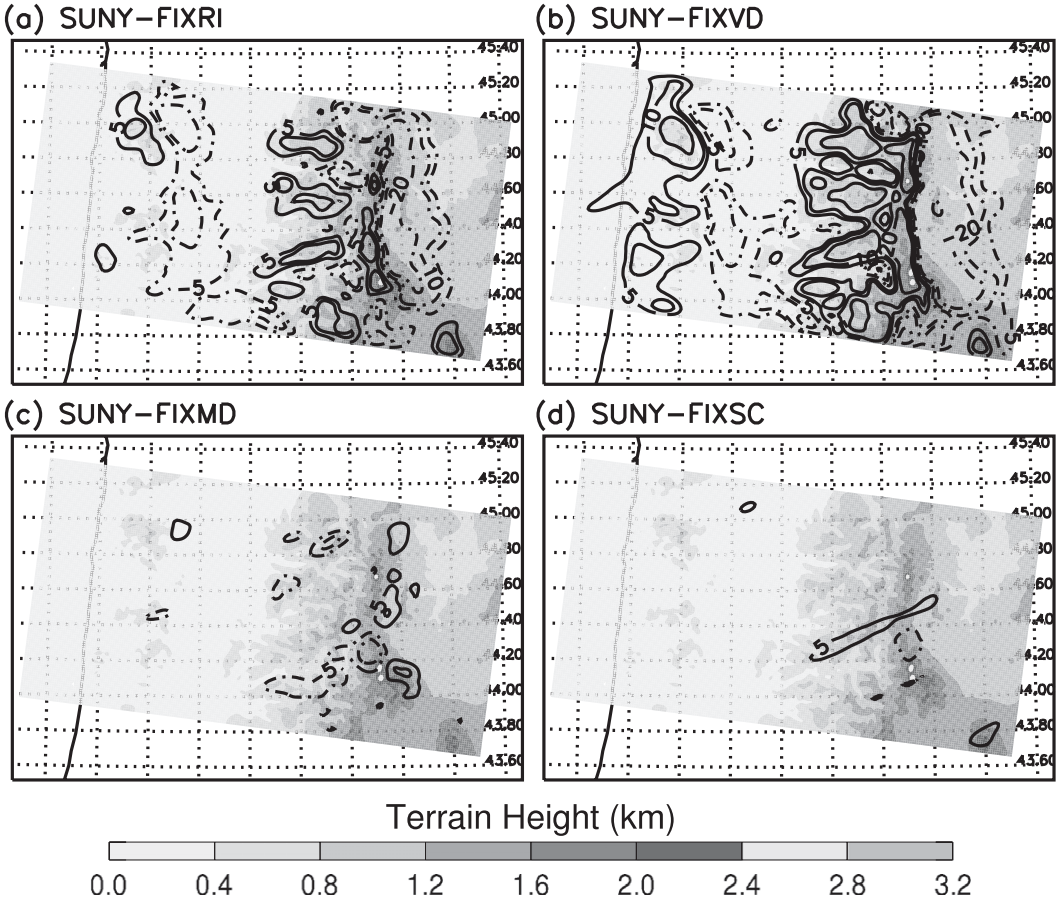

FIG. 20. As in Fig. 12b, but showing the precipitation difference between SBU-YLIN and the (a) fixed Ri run, (b) fixed *V-D* run, (c) fixed *M-D* run, and (d) fixed snow capacitance run.

are compared with observations and other BMPs in WRF. The new scheme predicts surface precipitation amounts comparable to those of other schemes. The new scheme reduces the IWC overprediction in the mixed phase part of the cloud and verifies better with aircraft in situ measurements, especially for the case with moderate riming aloft. Sensitivity tests suggest that reduced snow depositional growth and efficient fallout associated with the rimed snow ($Ri > 0$) yield the reduced snow aloft in the new scheme, with larger impact from the fallout. The new scheme has reasonable estimates of riming intensity as compared with aircraft estimates.

The new scheme needs to be further evaluated under different weather conditions and for large numbers of cases to have more robust results. Further evaluation of the new scheme will include some winter snowstorms over the U.S. Northeast, which will be reported in a future paper. Future work will also use more observations to better quantify Ri and its effect on the ice particle properties (area, mass, and fall velocity). These relationships are also important in microphysical retrievals from radar and satellite measurements. For example, all IWC retrieval algorithms need *A-D* and *M-D* to derive the IWC from radar reflectivity or satellite-measured radiance. Finally, the proposed formulation of ice particle properties is general enough to be easily implemented for any BMP, including double-moment schemes.

TABLE 3. Water budget results for a 3-h period (2300 UTC 13 Dec–0200 UTC 14 Dec) for the solid line box in Fig. 5c. The total surface precipitation within the box is in units of Tkg. The drying ratio (DR; in percent) is the ratio of the total precipitation within the solid line box in Fig. 5c and the moisture flux entering this box. The residence time (RT; in hundred of seconds) is the ratio of the total hydrometeors aloft and the surface precipitation rate within the box.

Simulation	Precipitation	DR (%)	RT (100s)
THOM1	241	18.1	26
THOM2	250	18.8	24
HUGH	274	19.9	23
SBU-YLIN	264	20.4	21

Acknowledgments. This research was supported by the National Science Foundation (Grants ATM-0450444 and 0908288) and the Office of Science (BER), U.S. Department of Energy (Lin). We thank Drs. Christopher Woods and David Kingsmill for processing the Convair and NOAA P-3 microphysical data. We appreciate the constructive comments by Drs. Yangang Liu, Greg Thompson, and Hugh Morrison. Use of WRF was made possible by the Microscale and Mesoscale Meteorological Division of the National Center for Atmospheric Research (NCAR), which is supported by the National Science Foundation. Comments from four anonymous reviewers greatly improved the manuscript.

APPENDIX

Description of Deposition and Autoconversion Parameterization

The parameterization is modified based on Lin et al. (1983) and Rutledge and Hobbs (1983), with the snow and graupel being combined and represented by PI using new *A-D*, *M-D*, and *V-D* relationships. We only present the parameterizations that are pertinent and different from other conventional parameterizations in this appendix. Herein P (kg kg^{-1} s^{-1}) represents the mass transformation rate.

a. Modification of PI depositional growth

PI deposition and sublimation with the consideration of latent heat release due to concurrent riming growth can be derived as (Kong and Yau 1997)

$$\frac{\partial m}{\partial t} = \frac{4\pi CFS_i}{g(t,p)} - \frac{L_s L_f}{KR_w T^2 g(t,p)}\left(\frac{\partial m}{\partial t}\right)_{\text{rim}}, \quad \text{(A1)}$$

where C is PI capacitance, F is the ventilation factor, S_i is the supersaturation with respect to ice, L_s is the latent heat of sublimation and L_f is latent heat of fusion, R_w is the gas constant for water vapor, K is air conductivity, and $g(t, p)$ is a thermodynamic quantity defined in Rogers and Yau (1989). Further, F is generally given, for example, by Thorpe and Mason (1966), as

$$F = 0.65 + 0.44S_c^{1/3}(\text{Re})^{0.5}, \quad \text{(A2)}$$

where S_c is the Schmidt number (equal to 0.6), Re is the Reynolds number defined before, and ν is kinematic viscosity of the air. The rate equation is integrated over the PI size spectrum assuming exponential distribution with intercept (N_{0s}) and slope (λ), and we get

$$P_{\text{sdep}} = \frac{4\pi CN_{0s}S_i}{g(t,p)}\left[\frac{0.65}{\lambda^2} + 0.44S_c\left(\frac{a_v}{\nu}\right)^{1/2}\left(\frac{\rho_0}{\rho}\right)^{1/4} \times \frac{\Gamma(2.5+0.5b_v)}{\lambda^{2.5+0.5b_v}}\right] - \frac{L_s L_f a_a a_v E_{s_c} N_{0s} q_w}{KR_w T^2 g(t,p)}\left(\frac{\rho_0}{\rho}\right)^{1/2} \times \frac{\Gamma(1+b_a+b_v)}{\lambda^{1+b_a+b_v}}. \quad \text{(A3)}$$

b. Autoconversion

Different Kessler-type parameterizations were compared and a new parameterization of autoconversion of cloud water to rain was derived by Liu and Daum (2004). The new parameterization is

$$P_{\text{wau}} = \left(\frac{3\rho}{4\pi\rho_w}\right)^2 \kappa_2 \beta_6^6 N^{-1} q_c^3 H(R_6 - R_{6c}), \quad \text{(A4)}$$

$$\beta_6^6 = \frac{(1+3\varepsilon^2)(1+4\varepsilon^2)(1+5\varepsilon^2)}{(1+\varepsilon^2)(1+2\varepsilon^2)}, \quad \text{(A5)}$$

$$R_{6c} = \beta_6 R_{3c}, R_6 = \beta_6 R_3, \quad \text{(A6)}$$

where the coefficient $\kappa_2 \approx 1.9 \times 10^{11}$ is in cm^{-3} s^{-1}, N is the cloud droplet number concentration, ε is the relative dispersion, and H is the Heaviside function to consider the threshold process such that the autoconversion rate is negligibly small when $R_6 < R_{6c}$; also, R_3 is the mean volume radius and R_{3c} is the threshold mean volume radius (generally set to 10 microns).

REFERENCES

Baker, B., and R. P. Lawson, 2006: In situ observations of the microphysical properties of wave, cirrus, and anvil clouds. Part I: Wave clouds. *J. Atmos. Sci.,* **63,** 3160–3185.

Barthazy, E., and R. Schefold, 2006: Fall velocity of snowflakes of different riming degree and crystal types. *Atmos. Res.,* **82,** 391–398.

Berry, E. X., 1968: Modification of the warm rain process. *Proc. First Conf. on Weather Modification,* Albany, NY, Amer. Meteor. Soc., 81–88.

——, and R. L. Reinhardt, 1974: An analysis of cloud drop growth by collection. Part IV: A new parameterization. *J. Atmos. Sci.,* **31,** 2127–2135.

Boudala, F. S., and G. A. Isaac, 2006: Replacing the Meyers et al. formula in bulk ice microphysics schemes in Canadian mesoscale models. *Extended Abstracts, 12th Conf. on Cloud Physics,* Madison, WI, Amer. Meteor. Soc., 2.5. [Available online at http://ams.confex.com/ams/Madison2006/techprogram/paper_111977.htm.]

Brown, P. R. A., and P. N. Francis, 1995: Improved measurements of the ice water content in cirrus using a total-water probe. *J. Atmos. Oceanic Technol.,* **12,** 410–414.

Chen, S.-H., and W.-Y. Sun, 2002: A one-dimensional time dependent cloud model. *J. Meteor. Soc. Japan,* **80,** 99–118.

Colle, B. A., and Y. Zeng, 2004: Bulk microphysical sensitivities within the MM5 for orographic precipitation. Part I: The Sierra 1986 event. *Mon. Wea. Rev.,* **132,** 2780–2801.

——, M. Garvert, J. B. Wolfe, C. F. Mass, and C. P. Woods, 2005: The 13–14 December 2001 IMPROVE-2 event. Part III: Simulated microphysical budgets and sensitivity studies. *J. Atmos. Sci.,* **62,** 3535–3558.

——, Y. Lin, S. Medina, and B. Smull, 2008: Orographic modification of convection and flow kinematics by the Oregon Coast Range and Cascades during IMPROVE-2. *Mon. Wea. Rev.,* **136,** 3894–3916.

Dudhia, J., S. Y. Hong, and K.-S. Lim, 2008: A new method for representing mixed-phase particle fall speeds in bulk microphysics parameterizations. *J. Meteor. Soc. Japan,* **86A,** 33–44.

Ferrier, B. S., 1994: A double-moment, multiple-phase, four-class bulk ice scheme. Part I: Description. *J. Atmos. Sci.,* **51,** 249–280.

Garvert, M. F., B. A. Colle, and C. F. Mass, 2005a: The 13–14 December 2001 IMPROVE-2 event. Part I: Synoptic and mesoscale evolution and comparison with a mesoscale model simulation. *J. Atmos. Sci.,* **62,** 3474–3492.

——, C. P. Woods, B. A. Colle, C. F. Mass, P. V. Hobbs, M. P. Stoelinga, and J. B. Wolfe, 2005b: The 13–14 December 2001 IMPROVE-2 event. Part II: Comparison of MM5 model simulations of clouds and precipitation with observations. *J. Atmos. Sci.,* **62,** 3520–3534.

——, B. F. Smull, and C. F. Mass, 2007: Multiscale mountain waves influencing a major orographic precipitation event. *J. Atmos. Sci.,* **64,** 711–737.

Grell, G. A., J. Dudhia, and D. R. Stauffer, 1994: A description of the fifth-generation Penn State/NCAR Mesoscale Model (MM5). NCAR Tech. Note NCAR/TN-398+STR, 138 pp.

Hahn, R. S., and C. F. Mass, 2009: The impact of positive definite moisture advection and low-level moisture flux bias over orography. *Mon. Wea. Rev.,* **137,** 3055–3071.

Hallett, M. F., and S. C. Mossop, 1974: Production of secondary ice particles during the riming process. *Nature,* **249,** 26–28.

Hanesch, M., 1999: Fall velocity and shape of snowflakes. Ph.D. thesis, Swiss Federal Institute of Technology, 117 pp.

Heymsfield, A. J., 2003: Properties of tropical and midlatitude ice cloud particle ensembles. Part I: Median mass diameters and terminal velocities. *J. Atmos. Sci.,* **60,** 2573–2591.

——, and L. J. Donner, 1990: A scheme for parameterizing ice-cloud water content in general circulation models. *J. Atmos. Sci.,* **47,** 1865–1877.

——, S. Lewis, A. Bansemer, J. Iaquinta, L. M. Miloshevich, M. Kajikawa, C. Twohy, and M. R. Poellot, 2002: A general approach for deriving the properties of cirrus and stratiform ice cloud particles. *J. Atmos. Sci.,* **59,** 3–29.

——, A. Bansemer, and C. H. Twohy, 2007: Refinements to ice particle mass dimensional and terminal velocity relationships for ice clouds. Part I: Temperature dependence. *J. Atmos. Sci.,* **64,** 1047–1067.

——, and Coauthors, 2008a: Testing IWC retrieval methods using radar and ancillary measurements with in situ data. *J. Appl. Meteor. Climatol.,* **47,** 135–163.

——, P. Field, and A. Bansemer, 2008b: Exponential size distributions for snow. *J. Atmos. Sci.,* **65,** 4017–4031.

Hong, S.-Y., and H.-L. Pan, 1996: Nonlocal boundary layer vertical diffusion in a medium-range forecast model. *Mon. Wea. Rev.,* **124,** 2322–2339.

——, and J.-O. J. Lim, 2006: The WRF Single-Moment 6-Class Microphysics Scheme (WSM6). *J. Korean Meteor. Soc.,* **42,** 129–151.

——, J. Dudhia, and S. H. Chen, 2004: A revised approach to ice microphysical processes for the bulk parameterization of clouds and precipitation. *Mon. Wea. Rev.,* **132,** 103–120.

Houze, R. A., P. V. Hobbs, P. H. Herzegh, and D. B. Parsons, 1979: Size distributions of precipitation particles in frontal clouds. *J. Atmos. Sci.,* **36,** 156–162.

Kain, J. S., 2004: The Kain–Fritsch convective parameterization: An update. *J. Appl. Meteor.,* **43,** 170–181.

——, and M. Fritsch, 1993: Convective parameterization for mesoscale models: The Kain–Fritsch scheme. *The Representation of Cumulus Convection in Numerical Models, Meteor. Monogr.,* No. 46, Amer. Meteor. Soc., 165–170.

Kessler, E., 1969: *On the Distribution and Continuity of Water Substance in Atmospheric Circulations*. *Meteor. Monogr.,* No. 32, Amer. Meteor. Soc., 84 pp.

Kong, F., and M. K. Yau, 1997: An explicit approach to microphysics in MC2. *Atmos.–Ocean,* **33,** 257–291.

Korolev, A. V., G. A. Isaac, and J. Hallett, 2000: Ice particle habits in stratiform clouds. *Quart. J. Roy. Meteor. Soc.,* **126,** 2873–2902.

——, ——, S. G. Cober, J. W. Strapp, and J. Hallett, 2003: Microphysical characterization of mixed-phase clouds. *Quart. J. Roy. Meteor. Soc.,* **129,** 39–65.

Li, G., Y. Wang, and R. Zhang, 2008: Implementation of a two-moment bulk microphysics scheme to the WRF model to investigate aerosol-cloud interaction. *J. Geophys. Res.,* **113,** D15211, doi:10.1029/2007JD009361.

Lin, Y., and B. A. Colle, 2009: The 4–5 December 2001 IMPROVE-2 Event: Observed microphysics and comparisons with the Weather Research and Forecasting model. *Mon. Wea. Rev.,* **137,** 1372–1392.

——, L. J. Donner, and B. A. Colle, 2011: Parameterization of riming intensity and its impact on ice fall speed using ARM data. *Mon. Wea. Rev.,* **139,** 1036–1047.

Lin, Y.-L., R. Farley, and H. D. Orville, 1983: Bulk parameterization of the snow field in a cloud model. *J. Climate Appl. Meteor.,* **22,** 1065–1092.

Liu, Y., 1995: On the generalized theory of atmospheric particle systems. *Adv. Atmos. Sci.,* **12,** 419–438.

——, and P. H. Daum, 2004: Parameterization of the autoconversion process. Part I: Analytical formulation of the Kessler-type parameterizations. *J. Atmos. Sci.,* **61,** 1539–1548.

Locatelli, J., and P. Hobbs, 1974: Fall speeds and masses of solid precipitation particles. *J. Geophys. Res.,* **79,** 2185–2197.

Mace, S. B., and Coauthors, 2006: Cloud radiative forcing at the Atmospheric Radiation Measurement Program Climate Research Facility: 1. Technique, validation, and comparison to satellite-derived diagnostic quantities. *J. Geophys. Res.,* **111,** D11S90, doi:10.1029/2005JD005921.

Meyers, M. P., R. L. Walker, J. Y. Harrington, and W. R. Cotton, 1997: New RAMS cloud microphysics parameterization. Part II: The two-moment scheme. *Atmos. Res.,* **45,** 3–39.

Milbrandt, J. A., and M. K. Yau, 2005: A multimoment bulk microphysics parameterization. Part II: A proposed three-moment closure and scheme description. *J. Atmos. Sci.,* **62,** 3065–3081.

——, ——, J. Mailhot, and S. Bélair, 2008: Simulation of an orographic precipitation event during IMPROVE-2. Part I: Evaluation of the control run using a triple-moment bulk microphysics scheme. *Mon. Wea. Rev.,* **136,** 3873–3893.

——, ——, ——, ——, and R. McTaggart-Cowan, 2010: Simulation of an orographic precipitation event during IMPROVE-2. Part II: Sensitivity to the number of moments in the bulk microphysics scheme. *Mon. Wea. Rev.,* **138,** 625–642.

Mitchell, D. L., 1996: Use of mass- and area-dimensional power laws for determining precipitation particle terminal velocities. *J. Atmos. Sci.,* **53,** 1710–1723.

——, R. Zhang, and R. L. Pitter, 1990: Mass-dimensional relationships for ice particles and the influence of riming on snowfall rates. *J. Appl. Meteor.,* **29,** 153–163.

Morrison, H., and W. W. Grabowski, 2008: A novel approach for representing ice microphysics in models: Description and tests using a kinematic framework. *J. Atmos. Sci.,* **65,** 1528–1548.

——, J. A. Curry, and V. I. Khvorostyanov, 2005: A new double-moment microphysics parameterization for application in cloud and climate models. Part I: Description. *J. Atmos. Sci.,* **62,** 1665–1677.

——, G. Thompson, and V. Tatarskii, 2009: Impact of cloud microphysics on the development of trailing stratiform precipitation in a simulated squall line: Comparison of one- and two-moment schemes. *Mon. Wea. Rev.,* **137,** 991–1007.

Mosimann, L., 1995: An improved method for determining the degree of snow crystal riming by vertical Doppler radar. *Atmos. Res.,* **37,** 305–323.

——, E. Weingartner, and A. Waldvogel, 1994: An analysis of accreted drop sizes and mass on rimed snow crystals. *J. Atmos. Sci.,* **51,** 1548–1558.

Pruppacher, H. R., and J. D. Klett, 1997: *Microphysics of Clouds and Precipitation*. 2nd ed. Kluwer Academic, 954 pp.

Reisner, J., R. M. Rasmussen, and R. T. Bruintjes, 1998: Explicit forecasting of supercooled liquid water in winter storms using the MM5 mesoscale model. *Quart. J. Roy. Meteor. Soc.,* **124,** 1071–1107.

Rogers, R. R., and M. K. Yau, 1989: *A Short Course in Cloud Physics.* Pergamon, 293 pp.

Rutledge, S. A., and P. V. Hobbs, 1983: The mesoscale and microscale structure and organization of clouds and precipitation in midlatitude cyclones. VIII: A model for the ''seeder-feeder'' process in warm-frontal rainbands. *J. Atmos. Sci.,* **40,** 1185–1206.

Schultz, P., 1995: An explicit cloud physics parameterization for operational numerical weather prediction. *Mon. Wea. Rev.,* **123,** 3331–3343.

Skamarock, W. C., 2006: Positive-definite and monotonic limiters for unrestricted-time-step transport schemes. *Mon. Wea. Rev.,* **134,** 2241–2250.

——, J. B. Klemp, J. Dudhia, D. O. Gill, D. M. Barker, W. Wang, and J. G. Powers, 2005: A description of the Advanced Research WRF, version 2. NCAR Tech. Note NCAR/TN-468+STR, 88 pp. [Available from UCAR Communications, P.O. Box 3000, Boulder, CO 80307.]

Stauffer, D. R., and N. L. Seaman, 1990: Use of four-dimensional data assimilation in a limited area mesoscale model. Part I: Experiments with synoptic-scale data. *Mon. Wea. Rev.,* **118,** 1250–1277.

Stoelinga, M., and Coauthors, 2003: Improvement of microphysical parameterization through observational verification experiments. *Bull. Amer. Meteor. Soc.,* **84,** 1807–1826.

——, H. McCormick, and J. D. Locatelli, 2007: Prediction of degree of riming within a bulk microphysical scheme. *Extended Abstracts, 22nd Conf. on Weather Analysis and Forecasting/18th Conf. on Numerical Weather Prediction,* Park City, UT, Amer. Meteor. Soc., 10B.1. [Available online at http://ams.confex.com/ams/22WAF18NWP/techprogram/paper_124851.htm.]

——, J. D. Locatelli, H. S. McCormick, and G. D. Casson, 2008: Climatology of crystal habits and degrees of riming for snow falling in the Cascade Mountains during two winter seasons. *Extended Abstracts, 13th Conf. on Mountain Meteorology,* Whistler, BC, Canada, 6A.2. [Available online at http://ams.confex.com/ams/13MontMet17AP/techprogram/paper_141394.htm.]

Stokes, G. M., and S. E. Schwartz, 1994: The Atmospheric Radiation Measurement (ARM) Program: Programmatic background and design of the cloud and radiation test bed. *Bull. Amer. Meteor. Soc.,* **75,** 1201–1221.

Straka, J. M., and E. R. Mansell, 2005: A bulk microphysics parameterization with multiple ice precipitation categories. *J. Appl. Meteor.,* **44,** 445–466.

Tao, W.-K., and J. S. Simpson, 1993: Goddard cumulus ensemble model. Part I: Model description. *Terr. Atmos. Ocean. Sci.,* **4,** 35–72.

——, ——, and M. McCumber, 1989: An ice-water saturation adjustment. *Mon. Wea. Rev.,* **117,** 231–235.

Thompson, G., R. M. Rasmussen, and K. Manning, 2004: Explicit forecasts of winter precipitation using an improved bulk microphysics scheme. Part I: Description and sensitivity analysis. *Mon. Wea. Rev.,* **132,** 519–542.

——, P. R. Field, R. M. Rasmussen, and W. D. Hall, 2008: Explicit forecasts of winter precipitation using an improved bulk microphysics scheme. Part II: Implementation of a new snow parameterization. *Mon. Wea. Rev.,* **136,** 5095–5115.

Thorpe, A. J., and B. J. Mason, 1966: The evaporation of ice spheres and ice crystals. *Br. J. Appl. Phys.,* **17,** 541–548.

Vidaurre, V., and J. Hallett, 2009: Particle impact and breakup in aircraft measurement. *J. Atmos. Oceanic Technol.,* **26,** 972–983.

Walko, R. L., W. R. Cotton, M. P. Meyers, and J. Y. Harrington, 1995: New RAMS cloud microphysics parameterization. Part I: The single-moment scheme. *Atmos. Res.,* **38,** 29–62.

Westbrook, C. D., R. J. Hogan, and A. J. Illingworth, 2008: The capacitance of pristine ice crystals and aggregate snowflakes. *J. Atmos. Sci.,* **65,** 206–219.

Woods, C. P., M. T. Stoelinga, J. D. Locatelli, and P. V. Hobbs, 2005: Microphysical processes and synergistic interaction between frontal and orographic forcing of precipitation during the 13 December 2001 IMPROVE-2 event over the Oregon Cascades. *J. Atmos. Sci.,* **62,** 3493–3519.

——, ——, and ——, 2007: The IMPROVE-1 Storm of 1–2 February 2001. Part III: Sensitivity of a mesoscale model simulation to the representation of snow particle types and testing of a bulk microphysical scheme with snow habit prediction. *J. Atmos. Sci.,* **64,** 3927–3948.

——, ——, and ——, 2008: Size spectra of snow particles measured in wintertime precipitation in the Pacific Northwest. *J. Atmos. Sci.,* **65,** 189–205.